Slow-down of the greening trend in natural vegetation with further rise in atmospheric CO_2

Alexander J. Winkler[1,2,3], Ranga B. Myneni[4], Alexis Hannart[5], Stephen Sitch[6], Vanessa Haverd[7,†], Danica Lombardozzi[8], Vivek K. Arora[9], Julia Pongratz[10,1], Julia E. M. S. Nabel[1], Daniel S. Goll[11], Etsushi Kato[12], Hanqin Tian[13], Almut Arneth[14], Pierre Friedlingstein[15], Atul K. Jain[16], Sönke Zaehle[3], and Victor Brovkin[1]

[1]Max-Planck-Institute for Meteorology, Bundesstrasse 53, 20146 Hamburg, Germany
[2]International Max-Planck Research School for Earth System Modeling, Bundesstrasse 53, 20146 Hamburg, Germany
[3]Max Planck Institute for Biogeochemistry, 07745 Jena, Germany
[4]Department of Earth and Environment, Boston University, Boston MA 02215, USA
[5]Ouranos, Montreal QC H2L 1K1, Quebec, Canada
[6]College of Life and Environmental Sciences, University of Exeter, Exeter EX4 4RJ, UK
[7]CSIRO Oceans and Atmosphere, Canberra, 2601, Australia
[8]Climate and Global Dynamics Laboratory, National Center for Atmospheric Research, Boulder, CO 80302, USA
[9]Canadian Centre for Climate Modelling and Analysis, Environment and Climate Change Canada, University of Victoria, Victoria, British Columbia, Canada V8W2Y2
[10]Department of Geography, Ludwig Maximilians University Munich, Luisenstr. 37, Munich D-80333, Germany
[11]Lehrstuhl fur Physische Geographie mit Schwerpunkt Klimaforschung, Universität Augsburg, Augsburg, Germany
[12]Institute of Applied Energy (IAE), Minato, Tokyo 105-0003, Japan
[13]International Center for Climate and Global Change Research, School of Forestry and Wildlife Sciences, Auburn University, 602 Duncan Drive, Auburn, AL 36849, USA
[14]Karlsruhe Institute of Technology, Institute of Meteorology and Climate Research/Atmospheric Environmental Research, Garmisch-Partenkirchen, Germany
[15]College of Engineering, Mathematics and Physical Sciences, University of Exeter, Exeter EX4 4QF, UK
[16]Department of Atmospheric Sciences, University of Illinois, Urbana, IL 61801, USA
[†]deceased, 19 January 2021

Correspondence: Alexander J. Winkler (alexander.winkler@mpimet.mpg.de *or* awinkler@bgc-jena.mpg.de)

Abstract. Satellite data reveal widespread changes of Earth's vegetation cover. Regions intensively attended to by humans are mostly greening due to land management. Natural vegetation, on the other hand, is exhibiting patterns of both greening and browning in all continents. Factors linked to anthropogenic carbon emissions, such as CO_2 fertilization, climate change and consequent disturbances, such as fires and droughts, are hypothesized to be key drivers of changes in natural vegetation. A

5   rigorous regional attribution at biome-level that can be scaled into a global picture of what is behind the observed changes is currently lacking. Here we analyze different datasets of decades-long satellite observations of global leaf area index (LAI, 1981-2017) as well as other proxies of vegetation changes, and identify several clusters of significant long-term changes. Using process-based model simulations (Earth system and land surface models), we disentangle the effects of anthropogenic carbon emissions on LAI in a probabilistic setting applying Causal Counterfactual Theory. The analysis prominently indicates the

10   effects of climate change on many biomes – warming in northern ecosystems (greening) and rainfall anomalies in tropical biomes (browning). ~~Our results provide only little support to previously published accounts of~~ The probabilistic attribution

method clearly identifies the CO_2 fertilization effect as the dominant driver in only two biomes, the temperate forests and cool grasslands, challenging the view of a dominant global-scale ~~effects of CO_2 fertilization~~effect. Altogether, our analysis reveals a slowing down of greening and strengthening of browning trends, particularly in the last two decades. Most models substantially underestimate the emerging vegetation browning, especially in the tropical rainforests. Leaf area loss in these productive ecosystems could be an early indicator of a slow-down in the terrestrial carbon sink. Models need to account for this effect to realize plausible climate projections of the 21st century.

1 Introduction

Satellite observations reveal widespread changes in terrestrial vegetation across the entire globe. The greening and browning trends reflect changes in the abundance of green leaves, and thus, the rate and amount of photosynthesis. Plants modulate pivotal land-atmosphere interactions through the process of photosynthesis. Hence, changes in photosynthetic activity have immediate effects on the land-atmosphere exchange of energy (Forzieri et al., 2017), water (McPherson, 2007; Ukkola et al., 2016) and carbon (Poulter et al., 2014; Thomas et al., 2016; Winkler et al., 2019a, b). Several studies have reported that many biomes are largely greening, from Arctic tundra to subtropical drylands (Myneni et al., 1997; Nemani et al., 2003; Mao et al., 2016; Zhu et al., 2016; Chen et al., 2019; Winkler et al., 2019a). Others have identified regions of declining trends in leaf area (Goetz et al., 2005; Verbyla, 2011). The drivers underlying these long-term vegetation changes, however, remain under debate. In the light of nearly forty years of continuous satellite observations, we reassess the driver attribution of natural vegetation changes in a new cause-and-effect framework.

Anthropogenic vegetation, *i.e.* actively cultivated vegetation, and natural vegetation should be considered separately due to their distinct origins and properties. A recent study by Chen et al. (2019) reported that anthropogenic vegetation (35% of the global vegetated area) is greening due to human land management. The authors identified irrigation, multiple cropping, and the application of fertilizers and pesticides as the main drivers of leaf area enhancement (direct drivers). These results challenge the conclusions of a previous study by Zhu et al. (2016) that attributed the global greening trend mostly to indirect drivers induced by CO_2 emissions, in particular, the CO_2 fertilization effect (70%).

Indirect drivers of vegetation changes usually include CO_2 fertilization and climatic change in the literature, both of which are consequences of rising atmospheric CO_2 concentration. The term "CO_2 fertilization" includes two effects of increased ambient CO_2 on the physiology of plants. First, elevated CO_2 in the interior of leaves stimulates carbon assimilation, which enhances plant productivity and biomass (Leakey et al., 2009; Fatichi et al., 2016). Second, leaves adapt to the CO_2-enriched atmosphere by lowering their stomatal conductance and ~~,~~potentially also their stomatal density over time, ~~stomatal density~~as *in-situ* observations suggest (Lammertsma et al., 2011). As a consequence, water loss through transpiration decreases, resulting in increased water-use efficiency (ratio of carbon assimilation to transpiration rate; Ukkola et al., 2016; Fatichi et al., 2016). In theory, both effects should result in an expansion of leaf area, especially in environments where plant growth is constrained by water availability (Donohue et al., 2009, 2013; Ukkola et al., 2016).

The radiative effect of CO_2 in the atmosphere induces climatic changes that can have both damaging or beneficial effects on the functioning of ecosystems. Temperature-limited biomes are expected to green (*i.e.* increase leaf area) due to warming and associated prolongation of the growing season (Park et al., 2016; Winkler et al., 2019a). But long-term drying (Zhou et al., 2014), as well as increased intensity and frequency of disturbances (Seidl et al., 2017) such as droughts (Bonal et al., 2016) and wildfires (Goetz et al., 2005; Verbyla, 2011), can induce regional vegetation browning trends. Regional greening and browning patterns can also be associated with insect outbreaks, local deforestation practices, regrowing or degrading forests, or nitrogen deposition; however, these drivers are considered to be of minor importance at the global scale (Zhu et al., 2016).

Indirect drivers affect both natural and anthropogenic vegetation unlike direct drivers which affect anthropogenic vegetation only. Chen et al. (2019) demonstrated that indirect drivers have either opposing or minor enhancing effects on the leaf area of anthropogenic vegetation. In general, the greening of anthropogenic vegetation has a negligible effect on the carbon cycle, because carbon absorbed by agricultural plants almost immediately ~~reenters~~ re-enters the atmosphere due to harvest and consumption. Natural terrestrial ecosystems, however, act as a strong carbon sink by absorbing about 30% of the anthropogenic CO_2 emissions (3.8±0.8 Pg C yr^{-1}; Quéré et al., 2018) and mitigate man-made climate change (Bonan, 2008; Sitch et al., 2015; Winkler et al., 2019a). Thus, a mechanistic understanding of natural vegetation dynamics under rising CO_2 is critical and helps to answer one of the key question in current climate research: *Where does the anthropogenic carbon go* (Marotzke et al., 2017)?

This study focuses on the response of natural vegetation under the influence of the two key indirect drivers, the physiological and radiative effect of rising CO_2. Throughout this paper and in accordance with literature, the terms "CO_2 fertilization" and "physiological effect of CO_2" are used interchangeably, as are "climate change" and "radiative effect of CO_2". To assess observed changes in vegetation over climatic time scales, we make use of a 37-year record of leaf area index (LAI) satellite observations (1982–2017, GIMMS LAI3g, Section 2.1). The GIMMS LAI3g product is based on the Advanced Very High Resolution Radiometer (AVHRR) sensors, for which there are a number of shortcomings (no on-board calibration, no correction of orbit loss, minimal correction for atmospheric contamination and limited cloud screening; Section 2.1; Zhu et al., 2013; Chen et al., 2019). To address these shortcomings, we also analyze a total of five different remote sensing products that pursue different strategies for dealing with the issues associated with AVHRR data (Section 2.1). Due to some inexplicable variations in these datasets (Forzieri et al., 2017) we concentrate on GIMMS LAI3g in our analysis, which is used in most published papers. Despite its limitations, the AVHRR record is unique in terms of its temporal coverage and offers an opportunity to study the evolution of Earth's vegetation while atmospheric CO_2 concentration increased by 65 ppm (341 to 406 ppm). We define greening and browning as statistically significant increasing and decreasing trends in LAI, respectively (Section 2.6). Based on a detailed biome map (Figure S1, Table S1, Section 2.2), we identify spatial clusters of significant vegetation greening and browning in different natural vegetation types.

We make use of the latest version of the fully-coupled Max Planck Institute Earth system model in ensemble-mode (MPI-ESM, Section 2.3) and a collection of 13 land-surface models (LSMs) driven with observed climatic conditions (TRENDYv7 ensemble; Section 2.4; Quéré et al., 2018). As a first step, we analyze historical simulations to examine whether these models capture the observed behavior of natural vegetation under rising CO_2. Next, we analyze factorial simulations to disentangle

and quantify the effects of rising CO_2 on LAI changes. Each factorial experiment consists of all historical forcings except one, which is set to its pre-industrial level (similar approach in TRENDYv7 simulations, for details see Section 2.4 and 2.6).

The conventional approach to detection and attribution in climate science is the method of optimal fingerprinting, for example as in Zhu et al. (2016). This framework which considers the observed change to be a linear combination of individual forced signals, is prone to overfitting, and assumes that linear correlation reflects causation (Hannart and Naveau, 2018). In particular, the attribution problem of the effects of increasing CO_2 is challenging in such an empirical regression setting, since "anything with a trend over the historical period will be correlated with increasing iCO_2" [increasing CO_2], as explained in a recent review article on the CO_2 fertilization effect (Walker et al., 2021). To overcome these limitations, we propose to use the Causal Counterfactual Theory which has recently been introduced to climate science (Pearl, 2009; Hannart et al., 2016; Hannart and Naveau, 2018). The method allows us to test if long-term greening/browning trends can be attributed to the effects of rising CO_2 in a probabilistic setting combining necessary and sufficient causation (Section 2.7).

This is the first study that addresses vegetation browning as well as greening patterns across all major biomes, integrated into a global picture. Greening is dominant in terms of areal fraction, but browning clusters are intensifying, primarily in the tropical forests that are biodiversity-rich and highly productive. We find that CO_2 fertilization is an important driver of greening in some biomes (temperate forests and cool grasslands), but cannot be established as a dominant causal driver in many others. The strengthening browning trend identified in our study is most likely linked to climate changes, *i.e.* long-term drying and recurring droughts. Overall, our findings suggest that the emerging browning clusters in the highly productive ecosystems might be a precursor of a weakening land carbon sink, which is not yet captured by the current land components of Earth system models.

2 Materials and Methods

2.1 Satellite observations of LAI

Our analyses are based on an updated version (V1) of the leaf area index dataset (LAI3g; Chen et al., 2019) based on the methodology developed by Zhu et al. (2013). The data provides global year-round LAI observations at 15-day (bi-monthly) temporal resolution and 1/12 degree spatial resolution. The record covers the period from July 1981 to December 2017. The complete time series of LAI3gV1 was generated using an artificial neural network trained on data of the overlap period of the Collection 6 Terra Moderate-Resolution Imaging Spectroradiometer (MODIS) LAI dataset (2000-2017) and and the latest version (third generation) of the Global Inventory Modeling and Mapping Studies group (GIMMS) Advanced Very High Resolution Radiometer (AVHRR) normalized difference vegetation index (NDVI) data (NDVI3g). The latter have been corrected for sensor degradation, inter-sensor differences, cloud cover, observational geometry effects due to satellite drift, Rayleigh scattering and stratospheric volcanic aerosols (Pinzon and Tucker, 2014).

The LAI3g datasets prior to 2000 were not evaluated due to a lack of required field data (Zhu et al., 2013; Chen et al., 2019). After 2000, the quality of the LAI3g dataset was assessed through direct comparisons with ground measurements of LAI and indirectly with other satellite-data based LAI products, and also through statistical analysis with climatic variables such as

temperature and precipitation variability (Zhu et al., 2013). Various studies used the predecessor LAI3gV0 and the related dataset of fraction of absorbed photosynthetically active radiation (FAPAR; Anav et al., 2013; Forkel et al., 2016; Zhu et al., 2016; Mao et al., 2016; Mahowald et al., 2016; Piao et al., 2014; Poulter et al., 2014; Keenan et al., 2016) and its successor
115 LAI3gV1 (Winkler et al., 2019a, b; Chen et al., 2019).

Leaf area index is defined as the one-sided green leaf area per unit ground area in broadleaf canopies and as one-half the green needle surface area in needleleaf canopies in both satellite observations and models (ESMs and LSMs). It is expressed in units of m^2 green leaf area per m^2 ground area. Missing values in the LAI3gV1 dataset are filled using the climatology of each 16-day composite during 1982-2017. We use the annual averaged LAI of each pixel in this study.

120 In addition to the GIMMS LAI3g product, we analyze the MODIS LAI record as well as four other long-term global remote sensing datasets: the Global Land Surface Satellites LAI product (GLASS LAI), the Global Mapping LAI product (GLOBMAP LAI), the NDVI product from the Land Long Term Data Record (LTDR), and a new FAPAR product from the National Oceanic and Atmospheric Administration's (NOAA) Climate Data Record Program.

The MODIS LAI data analysed in this study are based on the combined Terra and Aqua MODIS LAI products (MOD15A2H
125 and MYD15A2H) from Collection 6 (C6; Myneni et al., 2015a, b). These LAI datasets are provided at a 8-day temporal resolution with a 500 m sinusoidal projection covering the entire globe. ~~After additional data quality assessment (for more details, please see Chen~~ ~~, the~~ The two LAI datasets are aggregated into ~~a~~ 16-day composites by taking the mean of all valid LAI values after an additional data quality assessment is performed (for more details, please see Chen et al., 2019). The data are then spatially aggregated to 1/20 degree spatial resolution and cover the period from 2000 to 2019.

130 The GLASS LAI dataset (Xiao et al., 2014) is based on AVHRR, MODIS, and CYCLOPES reflectances and LAI products. The full time series was generated using an artificial neural network (general regression neural networks) that has been trained on the overlap period of AVHRR, MODIS and CYCLOPES reflectances and LAI products (Xiao et al., 2014). We use the latest version of the GLASS LAI dataset, which covers the period from 1981 to 2018 and is provided at a 8-day temporal and a 1/20 degree spatial resolution.

135 The GLOBMAP LAI dataset (Liu et al., 2012) is a reconstruction of the historical AVHRR data by a quantitative fusion with MODIS data. The algorithm inverses a geometrical optical model to establish pixel-level relationships between AVHRR and MODIS LAI for the overlapping period, which are then used to reconstruct AVHRR LAI back to the initial year of the record. We use the latest version of the GLOBMAP LAI dataset, which covers the period from 1981 to 2017 and is provided at a 15-day temporal and a 1/13.75 degree spatial resolution.

140 The NDVI dataset of NASA's LTDR (Pedelty et al., 2007) project is based on a reprocessing of long term AVHRR reflectances applying improved preprocessing techniques and atmospheric corrections used in the generation of MODIS datasets. The preprocessing improvements include radiometric in-flight vicarious calibration for the visible and near-infrared channels and inverse navigation to relate an Earth location to each sensor instantaneous field of view (Pedelty et al., 2007). Atmospheric corrections include corrections for Rayleigh scattering, ozone, water vapor, and aerosols. We use the recently published version
145 5 (v5) of the LTDR NDVI dataset, which covers the period from 1981 to 2019 and is provided at a daily temporal and a 1/20 degree spatial resolution.

The FAPAR product from the National Oceanic and Atmospheric Administration's (NOAA) Climate Data Record Program provided by National Centers for Environmental Information (NCEI) is based on carefully calibrated and corrected land surface reflectances from AVHRR sensors (Claverie et al., 2016). The algorithm relies on artificial neural networks calibrated per 150 different land cover types using the MODIS FAPAR dataset. We use the latest version of the FAPAR dataset from 1981 until 2019, which is provided at a daily temporal and a 1/20 degree spatial resolution.

We aggregate all data sets to annually averaged values and to spatially area-weighted averages for different biomes as defined by the mask (Section 2.2).

2.2 Characterization of biomes & clusters of significant change

155 The land cover product of the MODIS sensors (MCD12C1; MODIS/Terra and Aqua Combined Land Cover Type Climate Modeling Grid (CMG) Yearly Global 0.05 Deg V006, https://lpdaac.usgs.gov/dataset_discovery/modis/modis_products_table/mcd12c1_v006) is the primary source underlying the land cover map used in this study (hereafter MODIS land cover). The classes from the International Geosphere–Biosphere Programme (IGBP) in the MODIS land cover product are aggregated as follows: Tropical Forests include Evergreen Broadleaf Forest (EBF), Temperate Forests include Deciduous Broadleaf Forest 160 (DBF) and Mixed Forest, and Boreal Forests include Evergreen Needleleaf Forest (ENF) and Deciduous Needleleaf Forest (DNF). Savannas include Woody Savannas and Savannas. Shrublands include Closed Shrublands and Open Shrublands. Croplands include Croplands and Croplands / Natural Vegetation Mosaic. The class Others includes Permanent Wetlands, Urban and Built-up Lands, Permanent Snow and Ice, and Barren. The classes Grasslands and Water Bodies remain unchanged. The MODIS land cover product provides estimates for the time period from 2001 to 2017 for each pixel. In this study we define a 165 representative biome map based on the most frequently occurring land cover type throughout the period of 17 years.

The MODIS land cover classification does not contain the biome tundra, which is why we use in addition the land cover product GLDAS2 / Noah version 3.3 that uses a modified IGBP classification scheme providing the classes Wooded, Mixed or Bare Ground Tundra (https://ldas.gsfc.nasa.gov/gldas/GLDASvegetation.php, hereafter GLDAS land cover) (Rodell et al., 2004). Accordingly, pixels originally of the classes Shrublands, Grasslands, Permanent Wetlands, or Barren, are converted 170 to Tundra, if classified as Wooded, Mixed or Bare Ground Tundra in the GLDAS land cover product. The classes Woody Savannas and Savannas span vast areas across the globe in the MODIS land cover product. We use the GLDAS classification for these pixels, but only for regions where the MODIS and GLDAS land cover products disagree. In doing so, we obtain a more accurate global land cover classification. Table S1 describes in detail how the fusion of the MODIS and GLDAS land cover products is realized.

175 As a last step, we integrate the MODIS tree cover product MOD44B (MODIS/Terra Vegetation Continuous Fields Yearly L3 Global 250 m SIN Grid V006, https://lpdaac.usgs.gov/dataset_discovery/modis/modis_products_table/mod44b_v006) to account for the underestimation of forested area in the MODIS land cover product. Areas with tree cover exceeding 10% are formally defined as forests (MacDicken et al., 2015). Thus, we set non-forest pixels in the MODIS land cover product above 10% tree cover to Boreal Forest in the high latitudes 50° N/S. For tropical forest (25° S – 25° N), we increase the threshold to

20% tree cover to allow for a realistic areal extent of savannas. The pixels in the bands 25° N/S – 50° N/S remain unchanged, because the MODIS land cover product already realistically represents the forested area in these latitudes.

Table S1 provides a detailed overview on the conflation of MODIS land cover product, GLDAS land cover product and the MODIS Tree cover product. The final biome map (originally resolved at 0.05°) is regridded to the different resolutions of the AVHRR sensor and the models simulations (MPI-ESM and TRENDYv7) applying a largest area fraction remapping scheme.

Based on the observational LAI dataset we define various clusters for greening or browning in most biomes: North American Tundra (NAm Tundra), Eurasian Tundra (EA Tundra), North American Boreal Forests (NAm Brl F), Eurasian Boreal Forests (EA Brl F), Temperate Forests (Tmp F), Tropical Forests (Trp F), Central African Tropical Forests (CAf Trp F), Northern African Savannas and Grasslands (NAf Sv Gl), Southern African Savannas and Grasslands (SAf Sv Gl), Cool Grasslands (Cool Gl), and Australian Shrublands (Aus Sl). Some clusters require a more detailed definition of their geographical location and extent: Southern (Northern) African Savannas and Grasslands represent these vegetation type south (north) of the equator including Madagascar. Central African Tropical Forests represent all tropical forests in Africa. Cool Grasslands refer to grasslands above 30° N.

2.3 Max-Planck-Institute Earth System Model

MPI-ESM1.2 is the latest version of the state-of-the-art Max Planck Institute Earth System Model, which participates in the upcoming sixth phase of the Coupled Model Intercomparison Project (CMIP6; Eyring et al., 2016). Mauritsen et al. (2019) describes thoroughly the model developments and advancements with respect to its predecessor, the CMIP5 version (Giorgetta et al., 2013). Here, we use the low resolution (LR) fully coupled carbon/climate configuration (MPI-ESM1.2-LR), which consists of the atmospheric component ECHAM6.3 with 47 vertical levels and a horizontal resolution of ±200 km grid spacing (spectral truncation at T63). The ocean dynamical model MPIOM is set up on a bi-polar grid with an approximate grid-spacing of 150 km (GR1.5) and 40 vertical levels. MPI- ESM1.2-LR includes the latest versions of the land and ocean carbon cycle modules, comprising the ocean biogeochemistry model HAMOCC6 and the land surface scheme JSBACH3.2 (Mauritsen et al., 2019).

As opposed to the high-resolution configuration, the LR variant of the MPI-ESM includes all the important processes relevant for longer time-scale changes of the land surface, such as a thoroughly equilibrated global carbon cycle, dynamical vegetation changes, interactive nitrogen cycle, land-use transitions, a process-based fire model (SPITFIRE), and an interactive coupling of all sub-models. Furthermore, it is possible to run this model configuration to generate 45-85 model years per real-time day with a modern supercomputer (Mauritsen et al., 2019). This opens up the possibility of conducting a larger number of realizations for each experiment.

Specifically, we used the initial CMIP6 release of the MPI-ESM version 1.2.01 (mpiesm-1.2.01-release, revision number 9234). The final CMIP6 version will include further bug fixes, which are expected to only slightly influence long-term sensitivities of simulated land surface processes.

We conducted historical simulations (all forcings) and three factorial experiments (all forcings except one): (a) all historical forcings except the physiological effect of CO_2 (No PE; increasing CO_2 does not affect the biogeochemical processes), (b) all

historical forcings except the radiative effect of CO_2 (No RE; increasing CO_2 does not affect climate), and (c) all historical forcings except anthropogenic forcings (No CO_2). All experiments were preformed in ensemble-mode (6 realizations per experiment) using the latest CMIP6 forcing data (1850–2013). Individual realizations were initialized from different points in time of a prolongation run of the official MPI-ESM1.2-LR pre-industrial control simulation. In doing so, we account for the influence of climatic modes (e.g. El Niño Southern Oscillation) as a source of uncertainty in simulating long-term changes.

The simulated time series were shifted by four years to maximize the overlap with the observational record of 1982–2017.

2.4 Land surface models: TRENDYv7

Land-surface models (LSMs) or dynamic global vegetation models (DGVMs) simulate key physical and biological key processes of the land system in interaction with the atmosphere. LSMs provide a deeper insight into the mechanisms controlling terrestrial energy, hydrological and carbon cycles, as well as the drivers of phenomena ranging from short-term anomalies to long-term changes (Sitch et al., 2015; Bastos et al., 2018). Here, we analyze the most recent TRENDY ensemble (version 7) comprising 13 state-of-the-art LSMs which vary in their representation of ecosystem processes. All models simulate vegetation growth and mortality, deforestation and regrowth, vegetation and soil carbon responses to increasing atmospheric CO_2 levels, climate change and natural variability (Quéré et al., 2018). Some models simulate an explicit nitrogen cycle (allowing for potential nitrogen limitation) and account for atmospheric N deposition (Table A1 in Quéré et al., 2018). Most LSMs include the most important components of land-use and land-use changes, but they are far from representing all processes resulting from direct human land management (Table A1 in Quéré et al., 2018). A more detailed description of the TRENDYv7 ensemble, model-specific simulation setups and references can be found in Quéré et al. (2018, Table A4).

We use output from five simulations: all forcings (S3), physiological effect of CO_2 only (S1), radiative plus physiological effect of CO_2 (S2), land-use changes only (S4), and the control run (S0; no forcings: fixed CO_2 concentration of 276.59 ppm and fixed land-use map, loop of mean climate and variability from 1901–1920). The forcing data consist of observed atmospheric CO_2 concentrations, observed temporal patterns of temperature, precipitation, and incoming surface radiation from the CRU-JRA-55 reanalysis (Quéré et al., 2018; Harris et al., 2014), and human-induced land-cover changes and management from an extensions of the most recent Land-Use Harmonization (LUH2) dataset (Hurtt et al., 2011; Quéré et al., 2018).

In this study, we only analyze output for the period 1982–2017 (matching the observational record) from models providing spatially gridded data for all five simulations. A few models provide LAI at the level of plant functional types (PFTs). We calculate the average value of all LAI values on PFT level multiplied by their land cover fraction for each grid cell. All model outputs were spatially regridded to a common resolution of $1°$ based on a first-order conservative remapping scheme (Jones, 1999).

The design of factorial simulations in TRENDYv7 and by the MPI-ESM are conceptually different. The MPI-ESM simulations were conducted using the counterfactual approach, *i.e.* all forcings are present except the driver of interest. TRENDYv7 provides simulations with different combinations of drivers as described above. To obtain comparability, we have to make the assumption that the absence of a specific driver has the same effect, in absolute values, as its sole presence. Thus, we process the output of the simulations S1, S2, S3 and S4 to obtain the counterfactual setup as described above for MPI-ESM. This
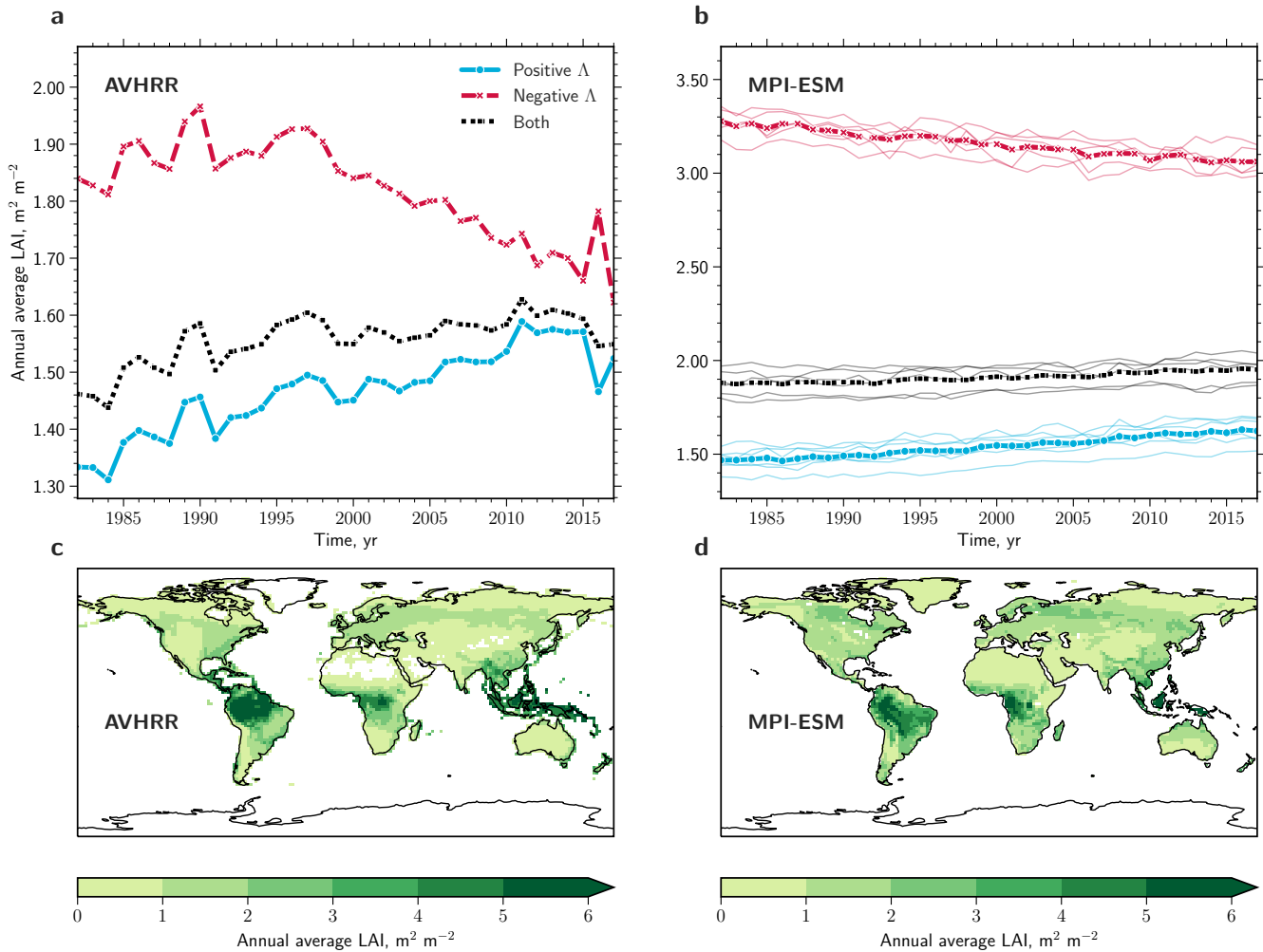
Figure 1. LAI observations versus MPI-ESM ensemble. a Time series of area-weighted annual average LAI for regions exhibiting positive (blue line) and negative trends (red line) masked for natural vegetation (denoted Λ). Black lines represent the overall signal of all pixels. **b** as **a**, but for the MPI-ESM. The individual realizations are represented as thin lines and the ensemble means are shown in bold lines. **c** Global patterns of annual average LAI over the time period 1982–2017 downscaled to MPI-ESM spatial resolution using first-order conservative remapping scheme (Jones, 1999). **d** as in **c**, but for the MPI-ESM.

approach neglects possible synergy effects from simultaneously acting forcings. Also, it has to be noted that these simulations are only to some extent comparable between the two ensembles. For instance, in the MPI-ESM we can specifically determine the impact of the radiative effect of CO_2, whereas TRENDYv7 uses observed atmospheric fields including changes induced from other drivers, such as non-CO_2 greenhouse gases.

For certain clusters, some models show unreasonable LAI changes and/or extreme inter-annual variability. To reduce the influence of these extreme models on the overall analysis, we apply a two-step filtering method for each cluster beforehand. Models are excluded from the analysis, if they exceed three times the inter-annual variability of observations and/or show a drastic change (of either sign) of more than 250% between the start and end of the observational period. Further, we apply a weighting scheme based on the performance of the all-forcings run for each cluster. We calculate quartic weights based on the distance between the simulated and observational estimate. These weights are applied when calculating the multi-model average and standard deviations for the factual and counterfactual runs.

2.5 Atmospheric CO_2 concentration

Global monthly means of atmospheric CO_2 concentration are taken from the GLOBALVIEW-CO2 product (for details see http://dx.doi.org/10.3334/OBSPACK/1002) provided by the National Oceanic and Atmospheric Administration/Earth System Research Laboratory (NOAA/ESRL).

2.6 Processing of the gridded data

Areas of significant change in LAI are estimated using the non-parametric Mann-Kendall test, which detects monotonic trends in time series. In this study, we set the significance level to $p \leq 0.1$. An alternative statistical test for trend detection (Cox-Stuart test; Sachs, 1997) yields approximately the same results. The trends are either calculated for time series on the pixel level or for area-weighted large-scale aggregated time series (e.g. biome level).

We define greening (browning) either as a positive (negative) temporal trend, or for better comparison among models and observations as well as for a better global comparison across diverse biomes, we express these trends relative to the initial LAI level at the beginning of the observational record (average state from 1982-1984), denoted as Λ (% decade^{-1}).

The calculation of yearly net changes in leaf area balances the effects from both statistically significant browning and greening grid cells. For each cell, we multiply the estimated trends by the respective grid area. The net change is the sum of all grid cells, where areas of insignificant change are set to zero.

Models fairly accurately reproduce global patterns of vegetation greening, however, the fraction of browning is considerably underrepresented. Yet, we can only consider pixels with significant negative trends in LAI, in observations and models alike, and test models with respect to driver attribution of browning trends. Thus, the attribution of browning trends in this paper exclusively refers to browning pixels only.

Models reveal biases in comparison to observations. To obtain informative results in the attribution analysis, we process the simulations to match the mean and variance of the observational time-series. Assuming additive and multiplicative biases in simulations, we apply the following corrections:

$$b = \frac{\sigma_{\mathrm{o}}}{\sigma_{\mathrm{af}}}, \tag{1}$$

$$a = \overline{x}_{\mathrm{o}} + b \times \overline{x}_{\mathrm{af}} \text{ , and} \tag{2}$$

$$y_{\mathrm{i}} = a + b * x_{\mathrm{i}} , \tag{3}$$

where $\overline{x}_{\mathrm{o}}$ represents the mean value and σ_{o} the standard deviation of the observational times series. $\overline{x}_{\mathrm{af}}$ and σ_{af} are analogous to the all-forcings simulations. All simulated time series x_{i} are scaled using equation 3, where $\mathrm{i} \in \Omega = \{\mathrm{factual\ runs, counterfactual\ runs}\}$. This processing step does not affect the nature of simulated trends.

2.7 Causal Counterfactual Theory

The causal counterfactual approach is anchored in a formal theory of event causation developed in computer science (Pearl, 2009; Marotzke, 2019). Recently, a framework for driver attribution of long-term trends in the context of climate change has been introduced (Hannart et al., 2016; Hannart and Naveau, 2018), and increasingly gains popularity (Marotzke, 2019). Through the use of this method we can ascertain the likelihood that a certain external forcing has caused an observed change in the Earth system. More precisely, we address the question of interest in a probabilistic setting, *i.e.* what is the probability that a given forcing (e.g. radiative effect of CO_2) has caused an observed long-term change in the system (e.g. greening of the Arctic).

In the following, we highlight the key ideas and relevant concepts of causal theory. A detailed description and formal derivations can be found in (Pearl, 2009; Hannart et al., 2016; Hannart and Naveau, 2018). We define the cause event (C) as "presence of a given forcing" (*i.e.* the factual world that occurred) and the complementary event ($\overline{C}$) as "absence of a given forcing" (*i.e.* the counterfactual world that would have existed in the absence of a given forcing; Hannart and Naveau, 2018). Further, we define the effect event (E) as the occurrence of a long-term change (here, greening or browning) and the complementary event ($\overline{E}$) as the non-occurrence of a long-term change (*i.e.* no persistent vegetation changes). In making use of numerical models, we can conduct factual runs comprising all forcings (*i.e.* historical simulations) as well as simulate counterfactual worlds by switching off a forcing of interest (*i.e.* all forcings except one). Based on an ensemble of simulations, either in a multi-model and/or multi-realizations setup, we derive the so-called factual (p_1) and counterfactual probability (p_0), which read $p_1 = P\{E|\mathrm{do}(C)\}$ and $p_0 = P\{E|\mathrm{do}(\overline{C})\}$, respectively (Hannart and Naveau, 2018). More precisely, p_1 describes

the probability of the event E in the real world where forcing C was present, whereas p_0 refers to the probability of the event E in a hypothetical world where forcing C was absent. The notation do($\cdot$) means that an *experimental intervention* is applied to the system to obtain the probabilities (Hannart and Naveau, 2018).

The three distinct facets of causality can be established based on the probabilities p_1 and p_0:

$$\text{PN} = \max\left\{1 - \frac{p_0}{p_1}, 0\right\}, \tag{4}$$

$$\text{PS} = \max\left\{1 - \frac{1 - p_1}{1 - p_0}, 0\right\}, \text{ and} \tag{5}$$

$$\text{PNS} = \max\left\{p_1 - p_0, 0\right\}. \tag{6}$$

PN refers to the probability of necessary causation, where the occurrence of E requires that of C but may also require other forcings. PS refers to the probability of sufficient causation, where the occurrence of C drives that of E but may not be required for E to occur. PNS describes the probability of necessary and sufficient causation, where PN and PS both hold (Hannart and Naveau, 2018). In other words, PNS may be considered as the probability that combines necessity and sufficiency. Thus, the main goal is to establish a high PNS that reflects and communicates evidence for the existence of a causal relationship in a simple manner (Hannart and Naveau, 2018).

To obtain PNS, we follow the methodology described in detail in Hannart and Naveau (Hannart and Naveau, 2018) and derive cumulative distribution functions (CDF) for the factual and counterfactual worlds, denoted D_0 and D_1, respectively. Assuming a Gaussian distribution, PNS follows as

$$\text{PNS} = \max\{D_1(\mu_1, \Sigma) - D_0(\mu_0, \Sigma)\}, \tag{7}$$

where μ_1 and μ_0 refer to the mean response of all factual and all counterfactual runs, respectively. Σ denotes the overall uncertainty and is estimated based on all simulations, comprising factual, counterfactual, and centuries-long unforced (pre-industrial) model runs (for details see Hannart and Naveau, 2018). Finally, the maximum of PNS determines the sought probability of causation (Hannart and Naveau, 2018). We express probabilities using the terminology and framework defined by the IPCC (Mastrandrea et al., 2011; Hannart and Naveau, 2018).

3   Results and Discussion

3.1   Natural vegetation exhibits a net gain of leaf area over the last decades, but the number of browning regions is increasing

More than three and half decades of satellite observations (1982–2017, Section 2.1) reveal that 40% of the Earth's natural vegetation shows statistically significant positive trends in LAI (Mann-Kendall test, $p < 0.1$; Table 1), concurrent with a 65 ppm increase in atmospheric CO_2. However, more and more browning clusters are beginning to emerge in all continents (14%; Table 1). Analyzing earlier versions of three shorter duration (1982-2009) LAI datasets, Zhu et al. (2016) reported a considerably smaller browning fraction of less than 4% and greening percentages ranging from 25% to 50% for all vegetation (*i.e.* including agriculturally dominated regions). The higher browning proportion in the extended record analyzed in this study indicates an intensification of leaf area loss in recent years. In the following, we take a closer look at different major biomes and their changes in LAI.

3.2   Earth's forests respond diversely throughout the satellite era

A global map of statistically significant trends in LAI (denoted Λ, Section 2.6) for natural vegetation reveals greening ($\Lambda > 0$) and browning ($\Lambda < 0$) clusters across the globe (Figure 2). Temperate forests ($\Lambda > 0$: 56%) and Eurasian boreal forests ($\Lambda > 0$: 53%) exhibit extensive regions of increasing LAI, and thereby, contribute the largest fraction to the enhancement of leaf area on the planet (Table 2). The global belt of tropical forests, on the other hand, while showing a net greening ($\Lambda > 0$: 28%), also feature widespread browning areas ($\Lambda < 0$: 16%). In particular, the Central African tropical forests contain large areas of pronounced negative trends ($\Lambda < 0$: 25%). North American boreal forests exhibit the largest fraction of browning vegetation ($\Lambda < 0$: 31%) resulting in an annual net loss of leaf area (Table 1 and 2). The picture of Earth's forests is generally in line with results based on other data sources. For instance, Song et al. (2018) reported a net gain of global forested area, with net loss in the tropics compensated by a net gain in the extra-tropics.

3.3   As in forests, other biomes also indicate divergent vegetation responses to rising CO_2

Tundra in North America is primarily greening ($\Lambda > 0$: 46% versus $\Lambda < 0$: 7%), whereas in Eurasia, browning is intensifying ($\Lambda > 0$: 35% versus $\Lambda < 0$: 20%), especially in northern Scandinavia and on the Taymar Peninsula in Northern Russia. Grasslands in cool arid climates, mainly comprising the Mongolian and Kazakh Steppe, as well as the Australian shrublands, stand out as prominent greening clusters ($\Lambda > 0$: 40% and 49%, respectively). Although these biomes show strong positive trends, they are characterized by a low level of LAI. The African continent, which is still dominated by natural vegetation, reveals a distinct change in leaf area. A greening band of savannas and grasslands in the northern regions of Sub-Saharan Africa and a greening cluster in Southern Africa border the browning regions of equatorial Africa (Figure 2). Overall, the response of LAI to rising CO_2 is somewhat homogeneous for some biomes (widespread browning of the tropical forests and dominant greening
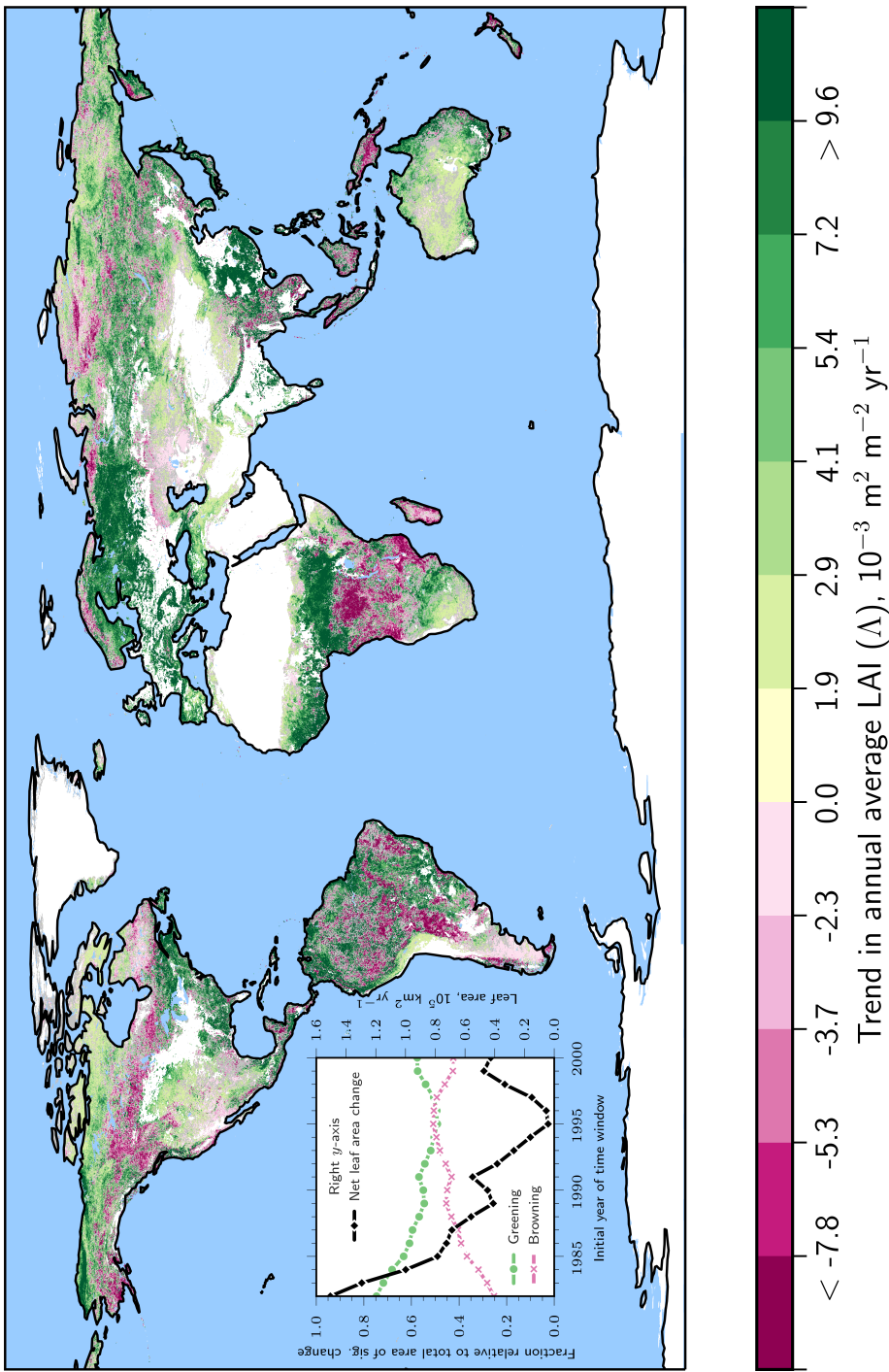
13

Figure 2. Natural vegetation exhibits patterns of opposing long-term LAI trends with rising CO_2. Global map of statistically significant (Mann-Kendall test, $p < 0.1$) annual average LAI trends (denoted Λ) for the entire period 1982–2017 (GIMMS LAI3g, color-coded). Areas of non-significant change are shown in gray. Anthropogenic vegetation (defined as croplands, Materials and Methods) is masked in white. Other white areas depict ice sheets or barren land. The inset line plot illustrates the change in fraction of positive (green dots) and negative Λ (red crosses) relative to the total area of significant change, and net leaf area change (black squares; right y-axis) for time windows of moving initial year (final year fixed at 2017). The x-axis shows the advancing initial year of the time window.

Table 1. Greening (positive Λ), browning (negative Λ) and non-changing fractions of vegetated area for different biomes and prominent clusters of change for the time period 1982–2017. Significant changes are determined by the means of the Mann-Kendall significance test (p < 0.1). The abbreviations used to describe the different clusters are explained in Materials and Methods.

Area	Vegetated Area	Positive Λ Fraction	Negative Λ Fraction	No-Change Fraction
Unit	$10^6 \ km^2$	-	-	-
All Vegetation	109.42	0.43	0.13	0.45
Anthro. Vegetation	15.37	0.6	0.07	0.32
Natural Vegetation	94.05	0.4	0.14	0.47
Biomes				
Grasslands	26.77	0.4	0.12	0.48
Tropical Forests	20.32	0.28	0.16	0.55
Boreal Forests	13.69	0.4	0.19	0.41
Temperate Forests	11.2	0.56	0.08	0.36
Shrublands	10.37	0.41	0.1	0.49
Tundra	7.03	0.41	0.14	0.45
Savannas	4.22	0.48	0.13	0.38
Clusters				
Cool Gl	12.32	0.4	0.12	0.48
EA Brl F	8.0	0.53	0.1	0.37
NAm Brl F	5.69	0.23	0.31	0.46
NAf Sv Gl	5.6	0.59	0.06	0.35
CAf Trp F	5.35	0.3	0.25	0.45
SAf Sv Gl	4.6	0.24	0.24	0.52
Aus Sl	4.43	0.49	0.03	0.49
EA Tundra	3.57	0.35	0.2	0.44
NAm Tundra	3.46	0.46	0.07	0.47

of the temperate forests), but divergent for others (tundra and boreal forests show a 'North America – Eurasia' asymmetry, interestingly, in that they show changes of reversed sign; Figure 2).

3.4 Net annual gain of leaf area is declining in natural vegetation

Leaf area loss occurs primarily in densely vegetated biomes (*i.e.* forests), which outweighs leaf area gain in rather sparsely vegetated regions (*i.e.* grasslands). For instance, vigorously greening areas of circumpolar tundra result in a leaf area gain of

8.74×10^3 km^2 yr^{-1}, which is almost outbalanced fourfold by a leaf area loss of 34.31×10^3 km^2 yr^{-1} in the browning regions of the tropical forests (Table 2). To assess the responses of different biomes to rising CO_2 in more detail, we iteratively calculate statistically significant LAI trends for different time windows with advancing initial year (*i.e.* 1982, 1983, ..., 2000), but fixed final year (2017). Although the estimated trends become less robust with shorter time series, this analysis allows us to test for weakening or strengthening responses to further rising CO_2. We see that the fraction of significantly browning regions is increasing over time, reaching a maximum for a time window starting in 1995. The greening fraction evolves in the opposite manner. The estimates are represented as fractions of the total area of significant change, because the latter inherently decreases as a result of the Mann-Kendall test for shorter time windows. Thus, the average annual net leaf area gain of 150.51 $\times 10^3$ km^2 yr^{-1} for the entire observational period (1982–2017) decreases with advancing initial year, approaching zero for the period 1995 to 2017, and rebounding to $\sim 40 \times 10^3$ km^2 yr^{-1} for the period 2000 to 2017 (black line in Figure 2 inset). To obtain comparability between different time windows, the net leaf area gain estimates were scaled to the total area of significant change derived for 1982–2017 (unprocessed estimates for period 2000–2017 are listed in Table S2). Chen et al. (2019) reported a global greening proportion of $\sim$ 33% (AVHRR: 21%; Table S2) and a browning proportion of only 5% (AVHRR: 13%; Table S2) analyzing the MODIS record including anthropogenic vegetation (2000–2017). On a global scale, LAI trends from MODIS and AVHRR agree over 61% of the vegetated area (Chen et al., 2019). Winkler et al. (2019b) analyzed in detail the AVHRR and MODIS LAI trends for different climate zones, vegetation classes, and latitudinal bands and found general agreement between the two satellite-based sensors. Inconsistencies arise mainly in humid tropical regions (e.g. absence of intensive browning in central African tropical forests in the MODIS record) and partially in the northern high latitudes (Chen et al., 2019). In Figure 5 we present a detailed comparison of different remote sensing datasets at the global scale and we elaborate further on the discrepancies among the estimates in Section 3.8 (for a similar analysis, also refer to Yuan et al., 2019).

3.5   High LAI regions are browning and low LAI regions are greening

The intensification of browning during the second half of the AVHRR observational period (2000–2017) results in a reversal of the sign in terms of net leaf area change in some biomes (*e.g.* tropical forests, North American boreal forests, and Eurasian tundra; Table S3). Critically, the tropical forests display the sharpest transition from a substantial net gain of 24.11×10^3 km^2 yr^{-1} (Table 2) to a comparably strong net loss of leaf area (-18.42 $\times 10^3$ km^2 yr^{-1}; Table S3). To address the temporal development of positive and negative changes in leaf area in more detail, we calculate time series of area-weighted averages of LAI (Figure 3a). We find that browning of natural vegetation occurs at a considerably higher level of LAI (on average $\sim$1.85) than greening (on average $\sim$1.32). Throughout the observational period, these two time series of opposite trends converge towards a LAI of 1.6 (Figure 3a). This convergence of greening and browning is not only evident in terms of their LAI level (Figure 3a), but also in their proportions (inset in Figure 2). The time series of anthropogenic vegetation on the other hand, aggregated for positive and negative Λ separately, are both confined to a comparable low LAI level (on average between 1 and 1.25). We next investigate the global LAI distributions of negative and positive changes and their development over time. Comparing distributions of the earlier (1982–1984) with those of the more recent years (2015–2017) reveals that browning primarily occurs at a high (5–6) and a medium level of LAI (1–2.5; Figure 3b). Greening, however, is occurring almost entirely

Table 2. Leaf area gain, loss, and net change for different biomes and prominent clusters of change for the time period 1982–2017. Significant changes are determined by the means of the Mann-Kendall significance test (p < 0.1). The abbreviations used to describe the different clusters are explained in Materials and Methods.

Leaf Area	Leaf Area Gain	Leaf Area Loss	Net Leaf Area Change
Unit	$10^3 \ km^2 \ yr^{-1}$	$10^3 \ km^2 \ yr^{-1}$	$10^3 \ km^2 \ yr^{-1}$
All Vegetation	296.87	-85.71	211.16
Anthro. Vegetation	67.12	-6.47	60.65
Natural Vegetation	229.75	-79.24	150.51
Biomes			
Grasslands	48.01	-12.51	35.50
Tropical Forests	58.42	-34.31	24.11
Boreal Forests	32.11	-14.45	17.66
Temperate Forests	53.32	-7.45	45.87
Shrublands	10.9	-2.4	8.50
Tundra	8.74	-3.69	5.05
Savannas	17.99	-4.21	13.78
Clusters			
Cool Gl	15.06	-3.75	11.31
EA Brl F	25.93	-4.26	21.67
NAm Brl F	6.18	-10.18	-4.00
NAf Sv Gl	23.42	-0.98	22.44
CAf Trp F	16.76	-13.76	3.00
SAf Sv Gl	5.51	-6.76	-1.25
Aus Sl	4.48	-0.16	4.32
EA Tundra	3.96	-3.04	0.92
NAm Tundra	4.78	-0.64	4.14

at low levels of LAI between 0–1.5. As a consequence, the global area-weighted averages of the browning and greening regions are approaching one another (dashed versus solid vertical lines in Figure 3b), as also depicted by the time series (Figure 3a). Overall, these results suggest a homogenization of Earth's natural vegetation in terms of LAI texture with rising CO_2. This homogenization becomes prominent when we compare the distributions of negative and positive Λ over time using a Q-Q plot (quantile-quantile; Figure 3c). The relationship between the quantiles is skewed to the left at higher LAI (positive Λ on *x*-axis, negative Λ on *y*-axis), because browning is prevalent in high LAI regions. Over time, the quantiles of the greening and browning distributions are approaching the 1-1 line (representing identical distributions), emphasizing their convergence.
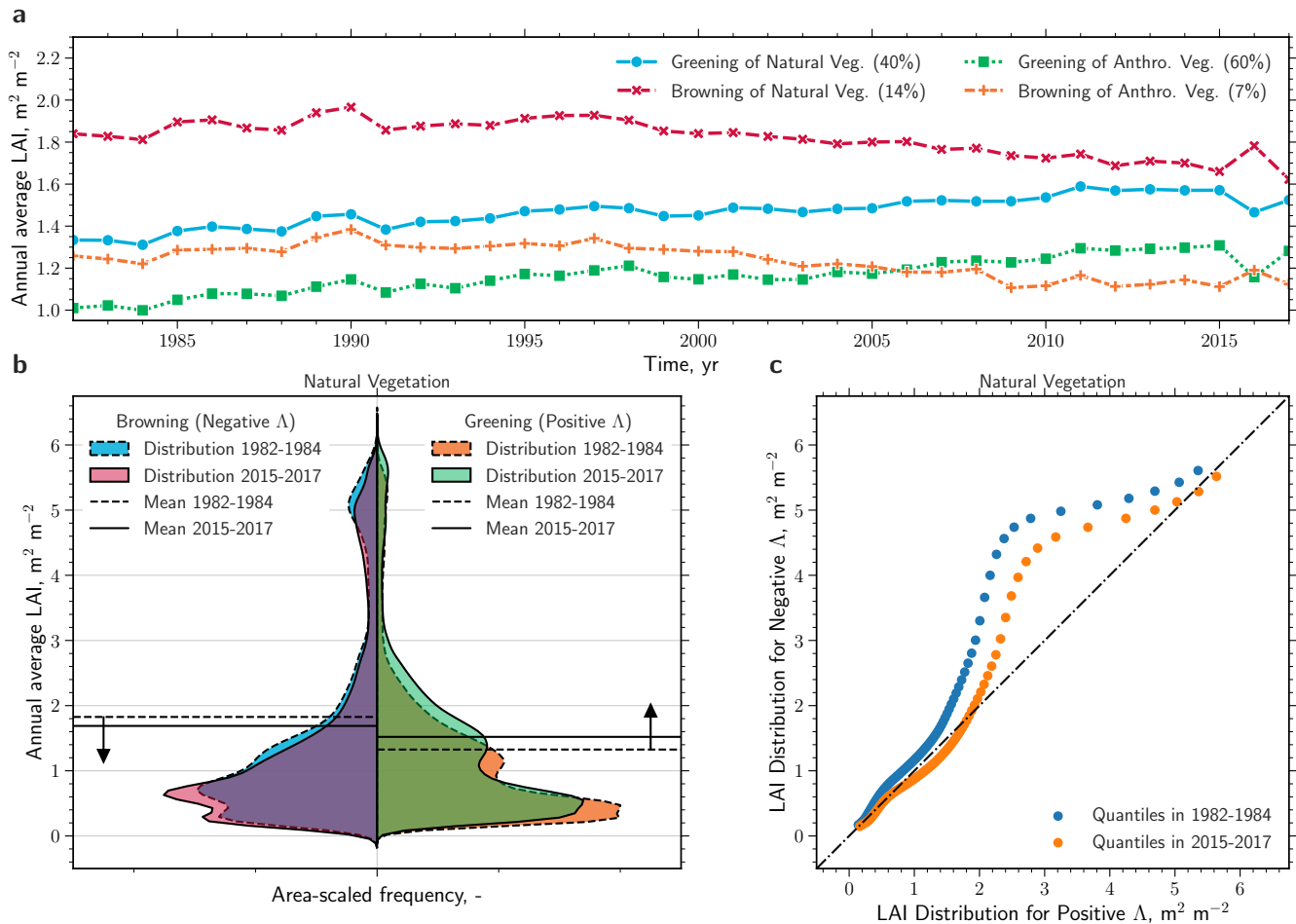
Figure 3. Observed homogenization of the global natural vegetation. a Time series of the area-weighted annual average LAI (GIMMS LAI3g, 1982–2017) of natural and anthropogenic vegetation for regions of positive (greening) and negative trends (browning). Only regions exhibiting significant trends are considered (Mann-Kendall significance test, $p < 0.1$) and are referred to as Λ. The percentages in brackets in the legend represent the respective proportions with respect to the total area. **b** Violin plot comparison of probability density functions (PDF, Gaussian kernel density estimation; all PDFs scaled to contain the same area) of LAI distributions of natural vegetation for negative (left) and positive Λ (right), and in time, 1982-1984 (dashed) versus 2015-2017 (solid). The horizontal lines represent the mean values for the respective period. **c** Q-Q (quantile-quantile) plot comparing the distributions of LAI for negative (*x*-axis) and positive Λ (*y*-axis) and their change over time, 1982-1984 (blue dots) versus 2015-2017 (orange dots).

3.6 The majority of models reproduce the observed convergence of greening and browning trends

Thus far, we have described the diverse long-term changes of natural vegetation across all continents and throughout the satellite era. We next investigate the underlying mechanisms driving these greening and browning trends and use the fully-coupled MPI-ESM and the TRENDYv7 ensemble of observation-driven LSMs (Section 2.3 and 2.4). First, we ask if these models capture

18

the observed behavior of natural vegetation under rising CO_2. MPI-ESM reproduces the observed browning of high LAI and
the greening of low LAI regions, however, the levels of LAI do not match the observations (Figure ~~S2).~~ 1a and b). Figure 1c
and d compare global maps of the observed and the simulated levels of annual average LAI. Overall, MPI-ESM is consistent
with observed patterns, with the strongest spatial variations in tropical forest regions. Historical simulations of TRENDYv7
(here 13 models) also show pronounced changes in vegetation, but exhibit a diverse behavior among the models (results not
shown for brevity). Seven LSMs reproduce observed converging trends of greening and browning, whereas the other six models
show divergent trends. All TRENDYv7 models are driven with identical atmospheric forcing fields, hence, these six models
most likely lack or incorrectly represent key processes of ecosystem functioning. In general, simulated greening patterns are
comparable to observations (Murray-Tortarolo et al., 2013; Sitch et al., 2015; Mahowald et al., 2016), but browning, especially
in the North American boreal forests, is underestimated (Sitch et al., 2015).

3.7 In an one-dimensional global perspective, models suggest the physiological effect of CO_2 as the main driver of greening

Hereafter, we use changes in annual average LAI relative to the baseline period 1982–1984 (Section 2.6) for better comparability between biomes, various simulations, and the observed signal. Time series of relative LAI changes from historical simulations (multi-model average for TRENDYv7 and multi-realizations average for MPI-ESM) are comparable to observations at the global scale (Figure 4a and 4b; temporal correlations are low due to high internal variability of the signal).

We use the framework of Counterfactual Causal Theory to attribute changes in LAI to a given driver in a probabilistic setting (Pearl, 2009; Hannart et al., 2016; Hannart and Naveau, 2018). Note that the causal relationships in this approach are determined based on the predictions of the models for the all-forcings (also referred to as factual) and factorial runs (also referred to as counterfactual), and therefore the causality results may reflect biases or misrepresentations in the models. Based on the factual and counterfactual runs, we derive **P**robabilities of causation that combines **N**ecessity and **S**ufficiency of each factor (PNS; see Section 2.7 for details). When aggregated to area-weighted global averages (*i.e.* Earth greening trend), the observed estimate (~ 1.08 % decade^{-1}) and the factual MPI-ESM estimate (~ 1.14 % decade^{-1}) are comparable, whereas the multi-model average of the TRENDYv7 ensemble is an overestimate (~ 1.79 % decade^{-1}; Figure 4c). Omitting CO_2-induced climate change (no radiative effect of CO_2, No RE) does not have a strong effect in the MPI-ESM (~ 1.04 % decade^{-1}), *i.e.* the estimate does not differ considerably from the factual run. The TRENDYv7 models indicate that the positive trend in LAI can be explained by climate change to some extent (~ 1.21 % decade^{-1}). However, the PNS values for the radiative effect of CO_2 are generally rather low (Fig. 4d), implying that the probability of the radiative effect of CO_2 acting as a sufficient and necessary causal driver of the globally aggregated LAI trend signal is rather low. The opposite is the case, when the physiological effect of CO_2 (No PE) is excluded. Both model setups agree that almost no positive trend in LAI is present in a world without the CO_2 fertilization effect (MPI-ESM: ~ 0.18 % decade^{-1}, TRENDYv7: ~ 0.08 % decade^{-1}; both estimates are lower than
~~internal variability~~ the overall uncertainty estimate of ~ 0.49 % decade^{-1}). Note that the term ~~variability~~ "overall uncertainty"
here refers to a broader concept of ~~variability~~ uncertainty that includes several components, such as climate variability, inter-

model variability, variability between realizations, and, if applicable, variability in observations, adapted from the approach introduced by Hannart and Naveau (2018, see also Section 2.7 for details).

As a consequence, high PNS can be established: The physiological effect of CO_2 has in the case of MPI-ESM *likely* (68%) and in the case of TRENDYv7 *very likely* (91%) caused the positive trend of global LAI in recent decades (Figure 4d). This result is in line with Zhu et al. (2016) who reported that 70% of global greening is attributable to CO_2 fertilization. Removing both effects of CO_2 results in slight negative trends, probably due to land use practices (e.g. deforestation; Figure 4c).

3.8 The global signal switches to a minor negative trend in the second half of the observational period

Natural vegetation shows a slight negative trend for the period 2000–2017 ($\sim$ -0.4 % decade^{-1}; Figure 4e). This estimate is within the range of ~~internal variability~~the overall uncertainty, and thus, should be interpreted with caution. Note, that the net change in leaf area is still positive when considering only significantly changing pixels (inset in Figure 2). To provide confidence in this result, we analyze three additional remote sensing datasets for LAI (MODIS-LAI, GLASS-LAI and GLOBMAP-LAI) as well as for the normalized difference vegetation index (LTDR-NDVI) and for the fraction of absorbed photosynthetic active radiation (NCEI-FAPAR), both proxies for leaf area changes (see Section 2.1 for details). We calculate time series of changes relative to the average baseline value from 1982-1984 to obtain comparability between the conceptually different estimates for changes in natural vegetation (Figure 5a-c). Next, we compare the trends for the entire observational period (1982–2017/2018, Figure 5d) with trends of the more recent past (2000–2018, Figure 5e). Three of the additional four long-term datasets show a weakening of vegetation greening for the second half of the observational period in accordance with the GIMMS LAI3g dataset (GLASS-LAI and especially LTDR-NDVI also show a reversal in the sign to a negative trend). In contrast, the dataset GLOBMAP-LAI depicts a substantial strengthening of the positive trend in LAI for the recent decades. However, the dataset also shows a suspicious jump in the year 2001, which could be an artifact related to problems in the fusion of the AVHRR and MODIS data (Piao et al., 2019). Furthermore, GLOBMAP-LAI generally shows the largest discrepancy among all datasets when compared to ground measurements (Xiao et al., 2017). The more short-term record of MODIS-LAI depicts a stable moderate greening trend for the time-span of 2000-2019. Since the MODIS record cannot provide any information on the state of the vegetation in the 1980s and 1990s, we cannot assess whether MODIS would also depict a slow-down of the overall greening trend over this time-period. Note that the comparability of relative trends between the long-term remote sensing products (baseline period 1982-1984) and short-term MODIS-LAI (baseline period 2000-2002) is limited. Overall, the analyses of the different remote sensing datasets support to a large extent the findings drawn from the GIMMS LAI3g dataset. For these reasons, and for reasons described earlier in the introduction, we focus on the GIMMS LAI3g dataset in these analyses, but we note that the single-product-centric view may imply some additional uncertainties besides the general uncertainty associated with AVHRR-based datasets.

Models reproduce the flattening of the trend and even the reversal in the sign only when the physiological effect of CO_2 is excluded or with a complete absence of CO_2 forcing (Figure 4e). A recent study by Wang et al. (2020) suggests that global CO_2 fertilization has declined in recent years by analyzing various observational datasets and highlights that land-surface models are not reproducing ~~this development~~the magnitude of this decline, mainly due to the under-representation of nutrient

limitation. While these results are consistent with ours, we are not convinced that one can infer a decline or saturation of the CO_2 fertilization effect from these observational datasets. Rather, we argue that countervailing effects associated with the radiative effect of increasing CO_2 (climatic changes, e.g., increase in atmospheric dryness and changes in water availability), as discussed below in more detail, become more pronounced and increasingly reduce vegetation productivity.

480   Overall, driver attribution at the global scale, as described above, and also in Zhu et al. (2016), neglects the heterogeneity of natural vegetation and the possibility that divergent responses of different natural biomes might cancel out. To account for this omission, we identify eleven clusters of significant change and derive probabilities of causation for each driver across different vegetation types (Figure 6).

3.9   Temperate forests prosper with rising CO_2 while tropical forests are increasingly under stress

485   Forests in temperate climates exhibit a strong positive trend in LAI (~ 2.53 % decade^{-1}), which is also seen in the models, albeit slightly overestimated (MPI-ESM: ~ 3.18 % decade^{-1}, TRENDYv7: ~ 2.69 % decade^{-1}; Figure ~~S3~~S2). The physiological effect of CO_2 is the main driver with high PNS (85% for MPI-ESM, 80% for TRENDYv7; Figure 6). The trends are slightly weaker when only analyzing the second half of the observational period, but the overall result does not change. Observed warming might have additionally contributed to enhanced vegetation growth (e.g. growing season extension; Piao

490   et al., 2011; Park et al., 2016), however, it is not identified as an important driver by models. Most temperate forests are in developed countries, and thus, have been managed in a sustainable manner for several decades (Currie and Bergen, 2008). It is conceivable, that some of the positive trends in LAI could be attributed to forest management or regrowing forests (Pugh et al., 2019), however, this is not captured by the models (*i.e.* trends are negative when complete CO_2 forcing is absent; Figure ~~S3~~S2).

495   The response of tropical forests to rising CO_2 is more complex. The signal over the entire observational period is slightly positive (~ 0.3 % decade^{-1}), however, it is within the range of ~~internal variability~~overall uncertainty. Therefore, no robust driver attribution is possible (Figure 6 and Figure ~~S4~~S3). TRENDYv7 models show strongly opposing responses of LAI to the different effects of CO_2: LAI decreases when the physiological effect is omitted, but increases when the radiative effect is omitted. MPI-ESM shows qualitatively the same responses, but less pronounced (Figure ~~S4~~S3). For the second half of the

500   satellite record, the observed trend switches sign to a strong negative trend (~ -1.4 % decade^{-1}). The models reproduce this tendency, but the multi-model average of the TRENDYv7 ensemble is still positive. During the same time period, the opposing reactions to CO_2 in the factorial runs are more strongly marked (Figure ~~S4~~S3). These results suggest that browning caused by CO_2-induced climate change is compensated by greening affiliated with the CO_2 fertilization effect at the biome level. Based on these findings, we hypothesize that the physiological effect of CO_2 is strong in models and outbalances the negative

505   effect of climate change in the tropical forests (Kolby Smith et al., 2016). As a consequence, the all-forcings simulations fail to reproduce the observed patterns of strengthening vegetation browning in the tropics (Zhou et al., 2014; Song et al., 2018). Because of the demonstrated limited predictive power of the models in simulating the vegetation response to climatic changes, we also rely more heavily on the published literature in the following discussion of our results.

3.10 Droughts and intensification of the dry season in the Amazon basin

510 The Amazonian tropical forests are being frequently afflicted by severe droughts. During the satellite era most of these droughts were strongly modulated by the El Niño Southern Oscillation (ENSO). For example, the droughts of 1982-83, 1987 and 1991–92 (Asner and Alencar, 2010; Anderson et al., 2018), 1997 (Williamson et al., 2000), and 2015-16 (Jiménez-Muñoz et al., 2016). The causes of the droughts in 2005 and 2010, however, were not related to ENSO, but rather to a warm anomaly in sea surface temperatures in the tropical North Atlantic (Marengo et al., 2008, 2011; Xu et al., 2011). Whereas the ENSO-

515 driven droughts peak in northern hemispheric winter, thus during the wet season, the non-ENSO droughts happened during the dry season (July – September), when tropical ecosystems are more vulnerable to negative rainfall anomalies.

These intense and frequent droughts have diverse impacts on tropical ecosystems (Bonal et al., 2016), the most prominent being an increase in wildfires and tree mortality. Recently, perennial legacy effects have been identified which lead to persistent biomass loss in the aftermath of severe droughts (Saatchi et al., 2013; Yang et al., 2018). For instance, some regions were still

520 recovering from the impact of the megadrought of 2005 when the next major drought began in 2010 (Saatchi et al., 2013). Maeda et al. (2015) found that these extreme events are also capable of disrupting hydrological mechanisms, which can lead to long-lasting changes in the structure of Amazonian ecosystems. Such droughts and associated wildfires are predicted to increase in frequency (Cai et al., 2014) and intensity (Fasullo et al., 2018) as a consequence of the ENSO-related amplification of heat waves, but also due to the projected warming of the tropical North Atlantic (Munday and Washington, 2019).

525 In addition to these episodic disturbances, long-term changes in climate also affected the tropical forests in the Amazon region. Rising surface air temperatures have considerably increased atmospheric water vapor pressure deficit (VPD), which has a negative effect on vegetation growth (Yuan et al., 2019). Moreover, we find that precipitation has steadily decreased during the dry season (July – September, Figure ~~S5 and S6~~S4 and S5) based on the latest version of the ECMWF reanalysis for the last forty years (ERA5; Dee et al., 2011). This rainfall deficit and the identified lengthening of the dry season (Fu et al.,

530 2013) exacerbate vegetation water stress during dry seasons and favor conditions for wildfires. The slight increasing trend in wet season precipitation (February – April) most likely cannot compensate for the water loss and its impact during the dry season (Figure ~~S5~~S4). Overall, the intensification of the dry season and the recurring droughts cause long-term browning trends (Xu et al., 2011), in line with our results of intensified browning of Amazonian forests (Figure ~~S6~~S5).

3.11 Drying trend in central African humid forests

535 African tropical forests have been experiencing a long-term drying trend since the 1970s (Malhi and Wright, 2004; Asefi-Najafabady and Saatchi, 2013; Zhou et al., 2014). In contrast to South America, the steady decline in rainfall is seen during both dry and wet seasons (Figure ~~S5~~S4). The origin of this decreasing trend in year-round rainfall is still under debate. Precipitation in equatorial Africa is expected to increase under climate change (Weber et al., 2018), so it is hypothesized that this trend is associated with the Atlantic Multidecadal Oscillation and/or changes in the West African Monsoon system (Asefi-Najafabady

540 and Saatchi, 2013). Long-term drying in rainforests could also be connected to the physiological effect of rising CO_2. Recently, it has been demonstrated that the reduction in stomatal conductance and transpiration induces a drier, warmer, and deeper

boundary layer, resulting in a decline in local rainfall (Langenbrunner et al., 2019). Regardless of what the causes may be, this long-term water deficiency most likely has led to the most pronounced cluster of vegetation browning in Earth's tropical forests ($\sim 174 \times 10^3$ km^2 net loss of leaf area in the time period of 2000–2017). No robust attribution is possible with the set of models
545 analyzed in this study, since they fail to capture this substantial decrease in leaf area in the all forcing runs (Figure ~~S7~~S6). In the case of the TRENDYv7 models, this finding is particularly noteworthy as they are driven with observed precipitation changes: The spatial patterns of negative trends in LAI and dry season precipitation in the Central African tropical forests coincide to a large extent (Figure ~~S5~~S4).

Interestingly, the MODIS record does not exhibit this browning cluster (Chen et al., 2019), though it has been reported in
550 other independent observational datasets (Zhou et al., 2014). Also, atmospheric CO_2 inversion studies have identified negative trends in carbon uptake for this region (Fernández-Martínez et al., 2019), which corroborates our results based on the LAI3g dataset.

3.12 Tropical forests in Oceania are afflicted by deforestation

Although we exclude direct anthropogenic land-cover changes (Figure S1, Table S1) as well as abrupt changes (Mann-Kendall
555 test for monotonic trends, Section 2.6), the LAI trend maps nevertheless show characteristic deforestation patterns, e.g. the so-called "arc of deforestation" in the Amazon region ~~(Figure S6; Aldrich et al., 2012)~~(Figure S5; Aldrich et al., 2012). Hence, deforestation practices may explain some part of the observed gradual browning of the Amazon (Song et al., 2015) and African tropical forests (Mayaux et al., 2013; Tyukavina et al., 2018).

In Oceania, however, deforestation appears to be a crucial driver of the observed browning in the pristine tropical forests.
560 Significant negative trends align strongly with patterns of drastic deforestation during recent decades, described in detail by Stibig et al. (2014, in comparison to Figure 2). As opposed to Central Africa and the Amazon region, climate changes are unlikely to be the key driver of browning regions in Oceania. There, precipitation, although highly variable in the dry season, appears to increase (Figure ~~S5~~S4) and the increase in VPD is rather minor in tropical forests (Yuan et al., 2019).

3.13 Climate change drives an asymmetrical development of North American and Eurasian ecosystems

565 The boreal forests show strong positive trends in Eurasia (Observations: ~ 2.69 % decade^{-1}, MPI-ESM: ~ 3.48 % decade^{-1}, and TRENDYv7: ~ 2.08 % decade^{-1}), which can mostly be attributed to amplified warming of the temperature-limited northern high latitudes (PNS = 71% for TRENDYv7, PNS = 44% for MPI-ESM; Figure ~~S8~~S7). North American boreal forests exhibit a negative response to the effects of rising CO_2, which has amplified over the last two decades ($\sim$ -0.95 % decade^{-1}, 2000–2017). Models do not reproduce the dominant browning pattern (Figure ~~S9~~S8), which is most likely connected to in-
570 adequate representation of disturbances (Sitch et al., 2015). Several studies have proposed that browning has occurred as consequence of droughts, wildfire, and insect outbreaks in the North American boreal forests (Goetz et al., 2005; Sitch et al., 2015; Beck and Goetz, 2011; Kurz et al., 2008). Macias Fauria and Johnson (2008) showed that the frequency of wildfires is strongly related to the dynamics of large-scale climatic patterns (Pacific Decadal Oscillation, El Niño Southern Oscillation, and Arctic Oscillation) and thus, cannot be tied conclusively to anthropogenic climate change. However, there is also evidence

that the residing tree species suffer from drought stress induced by higher evaporative demand as the temperature rises (Verbyla, 2011). Moreover, models lack a representation of the asymmetry in tree species distribution between North America and Eurasia, which could explain their divergent reactions to changes in key environmental variables (Abis and Brovkin, 2017). Further observational evidence for the browning of North American boreal forests and the associated decline in net ecosystem productivity can also be inferred from CO_2 inversion products (Fernández-Martínez et al., 2019; Bastos et al., 2019).

Tundra ecosystems also reveal a dipole-type development between North America and Eurasia, however with a reversed sign. Hence, North American tundra is strongly greening (Observations: ~ 4.23 % decade^{-1}, MPI-ESM: ~ 4 % decade^{-1}, and TRENDYv7: ~ 4.51 % decade^{-1}), which is *virtually certain* (PNS = 99% for TRENDYv7) and *about likely as not* (PNS = 51% for MPI-ESM) caused by warming (Figure S10S9). The trend decreases for the period 2000–2017, which could be linked to the warming hiatus in the years 1998–2012 (Bhatt et al., 2013; Ballantyne et al., 2017; Hedemann et al., 2017). This is in line with the observed slow down in tundra greening due to short-term cooling after volcanic eruptions (Lucht et al., 2002).

Eurasian tundra show a positive trend for the years 1982–2017, but a reversal in trend sign for the years 2000–2017 (Figure S11S10). Models exhibit some evidence of a strengthening browning signal, but fail to capture the full extent of the emerging browning clusters seen in observations. If we only consider the grid cells that show significant browning in observations and models, we are able to conduct a robust driver attribution. According to the TRENDYv7 ensemble, the browning cluster in Eurasian tundra can *very likely* be attributed to CO_2 induced climate change (PNS = 93%, PNS = 47% for MPI-ESM). These results are in line with studies showing that tundra ecosystems are susceptible to warm spells during growing season (Phoenix and Bjerke, 2016) and to frequent droughts (Beck and Goetz, 2011). The asymmetry between Eurasia and North America can be explained by changes in large-scale atmospheric circulation. Eurasia is cooling through increased summer cloud cover, whereas North America is warming through more cloudless skies (Bhatt et al., 2013, 2014). Also linkages between regional Arctic sea ice retreat, subsequent increasing ice-free waters, and regional Arctic vegetation dynamics have been postulated (Bhatt et al., 2014).

3.14 Vegetation in arid climates is greening, except in South America

Non-forested greening clusters beyond the high northern latitudes coincide with semi-arid to arid climates (Park et al., 2018). The Northern Sub-Saharan African savannas and grasslands greened extensively in recent decades (~ 4.63 % decade^{-1}; Figure S12S11), which is reproduced by the observation-driven TRENDYv7 models (~ 4.55 % decade^{-1}), and is *likely* caused by climatic changes (PNS = 68%). No robust attribution is feasible based on the MPI-ESM simulations. However, it is noteworthy, that the fully-coupled Earth system model points to climate change as having a negative effect in these regions, thus, not reproducing the observed increase in rainfall (Figure S12S11). This provides evidence for the hypothesis that African precipitation anomalies are not induced by rising CO_2, but rather follow a multidecadal internal climatic mode (Asefi-Najafabady and Saatchi, 2013).

Internal variability The overall uncertainty in LAI changes is strong high in the Southern African grasslands and savannas, and thus, no robust long-term change can be identified (Figure S13S12). It has been shown that shrublands in the more southern regions are greening in response to increased rainfall (Fensholt and Rasmussen, 2011). In general, the literature suggests that

greening and browning patterns in arid climates are mainly driven by precipitation anomalies (Fensholt and Rasmussen, 2011; Fensholt et al., 2012; Gu et al., 2016; Adler et al., 2017). Close resemblance arises when comparing the spatial patterns of precipitation trends throughout the satellite era (Adler et al., 2017) with significant changes in vegetation in arid environments, especially so in the African continent. Decreased rainfall in arid South America coincides with strong browning clusters (Fensholt et al., 2012). This is in disagreement with the expected strong manifestation of CO_2 fertilization in water-limited environments (Ukkola et al., 2016).

Australian Shrublands show a persistent positive LAI trend ($\sim$ 3.84 % decade^{-1}), intermittently perturbed by climatic extreme events ~~(e.g. strong anomalous rainfall with subsequent extensive vegetation greening in 2011, Figure S14; Poulter et al., 2014)~~ (e.g. strong anomalous rainfall with subsequent extensive vegetation greening in 2011, Figure S13; Poulter et al., 2014). Models reproduce the steady greening of Australia, but no robust driver attribution is feasible due to ~~strong internal variability~~high overall uncertainty. However, both model setups point to the physiological effect of CO_2 as the dominant driver (Figure ~~S14~~S13). These results are congruent with recent studies (Donohue et al., 2009; Ukkola et al., 2016) that show CO_2 fertilization enhanced vegetation growth by lowering the water limitation threshold.

Grasslands in the cool arid climates exhibit persistent positive trends ($\sim$ 2.03 % decade^{-1}, Figure ~~S15~~S14). Simulated estimates are in the range of the observations (MPI-ESM: $\sim$ 2.33 % decade^{-1} and TRENDYv7: $\sim$ 1.81 % decade^{-1}). Our analysis suggests that the positive response of cool arid grasslands to rising CO_2 can be explained by the physiological effect of CO_2 (PNS = 85% for TRENDYv7, PNS = 88% for MPI-ESM). These ecosystems are dominated by C_3-type plants (Still et al., 2003), which are susceptible to CO_2 fertilization (Sage et al., 2012), thus, consistent with our results. In the warm arid areas, C_4-type grasses dominate (Still et al., 2003), which are less sensitive to the physiological effects of CO_2 (Sage et al., 2012). As discussed above, vegetation changes there are mostly driven by precipitation anomalies, although CO_2 fertilization might also contribute to a limited extent (Sage et al., 2012).
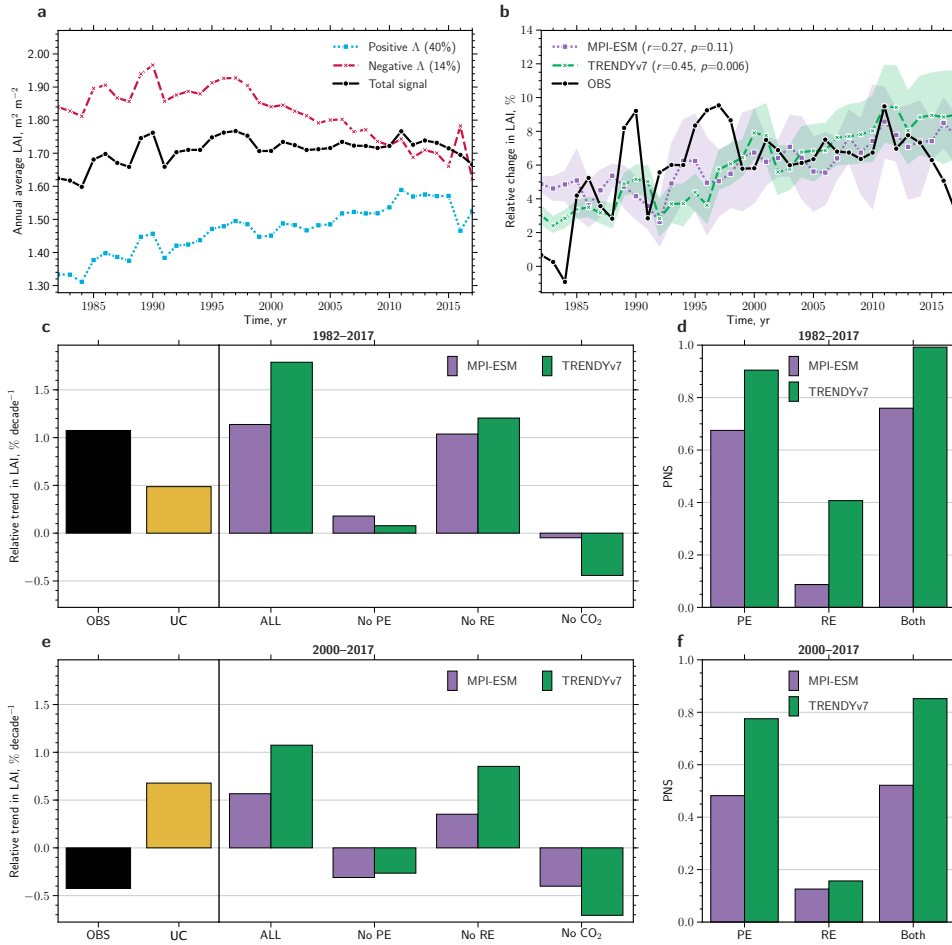
Figure 4. Driver attribution of changing natural vegetation at the global scale: neglecting ecosystem heterogeneity could lead to misleading results. a Time series of the area-weighted annual average LAI (GIMMS LAI3g, 1982–2017) for regions of positive (blue dotted line) and negative sensitivity (red dashed line) to rising atmospheric CO_2 concentration (Λ) of natural vegetation. Black solid line represents the overall signal of all pixels. The percentages in brackets in the legend represent the greening and browning proportions with respect to the total area. **b** Time series of changes in LAI relative to the average state from 1982–1984, comparing observations (black solid line) with historical simulations, where the green dashed line denotes the ensemble mean of 13 offline-driven land surface models (TRENDYv7, Data and Methods), and the purple dotted line denotes the average of an ensemble of multi-realizations with a fully-coupled Earth system model (MPI-ESM, Data and Methods). The colored shading represents the 95% confidence interval estimated by bootstrapping. The correlation coefficients (including significance level) of the observed and simulated time series are displayed in brackets in the legend. **c** Bar chart showing relative trends in LAI (in % yr^{-1}) of the total observed signal (black) and for factual (all historical forcings; ALL) as well as for counterfactual simulations, i.e. no historical CO_2 forcing (No CO_2), all historical forcings except the physiological effect (No PE) or the radiative effect (No RE) of atmospheric CO_2, as estimated by TRENDYv7 (green) and MPI-ESM (purple). The yellow bar represents ~~internal variability~~ the overall uncertainty (~~IV~~UC) including inter-model variations derived from all simulations (control, factual and counterfactual). **d** Probabilities of necessary and sufficient causation (PNS) of the change in LAI, comparing the physiological (PE) and radiative effect (RE) of CO_2 as well as their combined effect (Both). **e** as in **c** but for the period 2000–2017. **f** as in **d** but for the period 2000–2017.
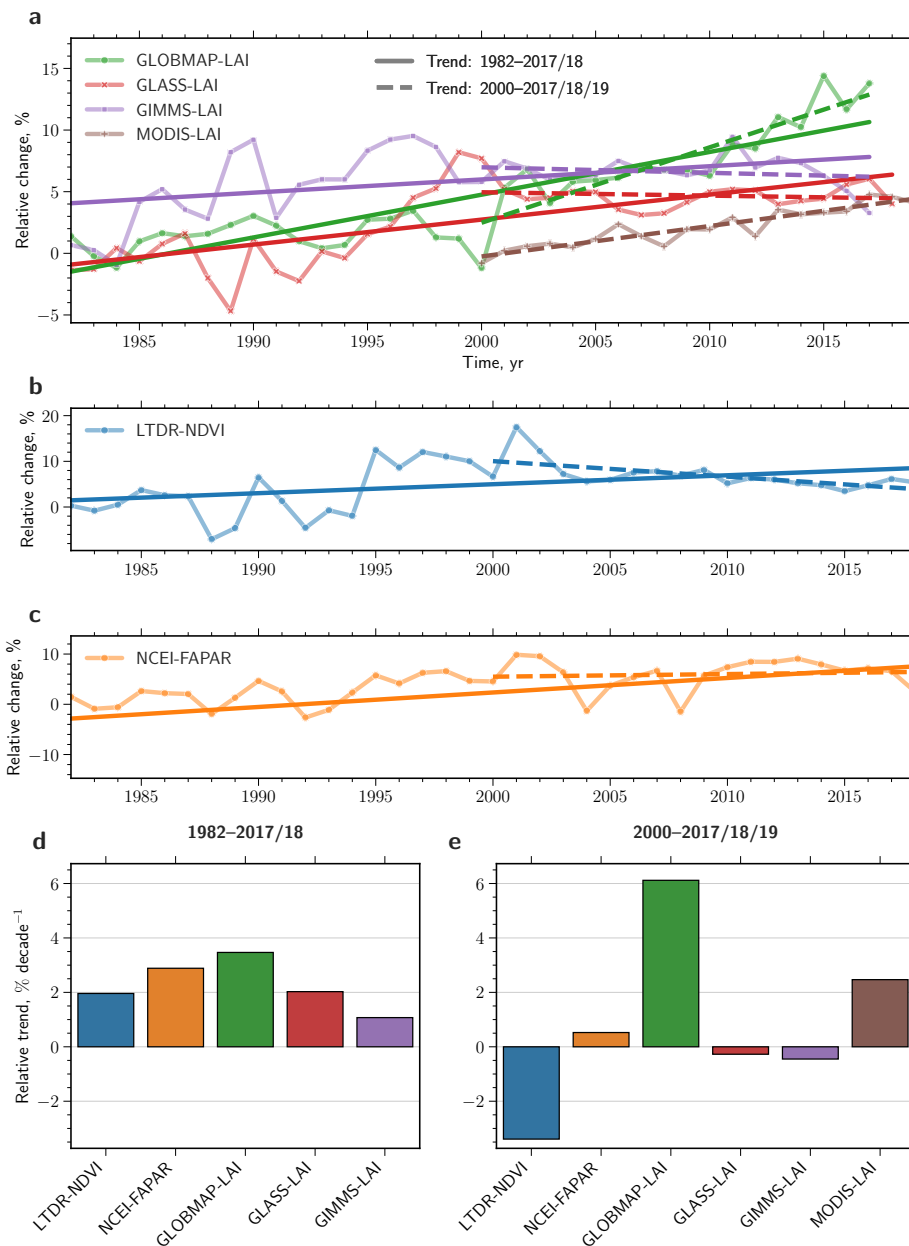
26

Figure 5. Five different remote sensing datasets displaying the development of natural vegetation over the last four decades. a Time series of changes in LAI relative to the average state from 1982–1984 as depicted in three different datasets (green: GLOBMAP-LAI, red: GLASS-LAI, purple: GIMMS-LAI and brown: MODIS-LAI; see Materials and Methods section of the main paper for further details). The solid straight line represents the best linear fit for the entire period (1982–2017/2018), the dashed line represents the best linear fit for the second half of the period (2000–2017/18/19). **b** as in **a** but for the dataset LTDR-NDVI (blue; see Materials and Methods section of the main paper for further details). **c** as in **a** but for the dataset NCEI-FAPAR (orange; see Materials and Methods section of the main paper for further details). **d** Bar chart comparing relative trends (in % decade^{-1}) in LAI, NDVI and FAPAR from different datasets for the entire period (1982–2017/2018) obtained from the gradients shown in **a-c**, respectively. **e** as in **d** but for the second half of the period (2000–2017/18/19).
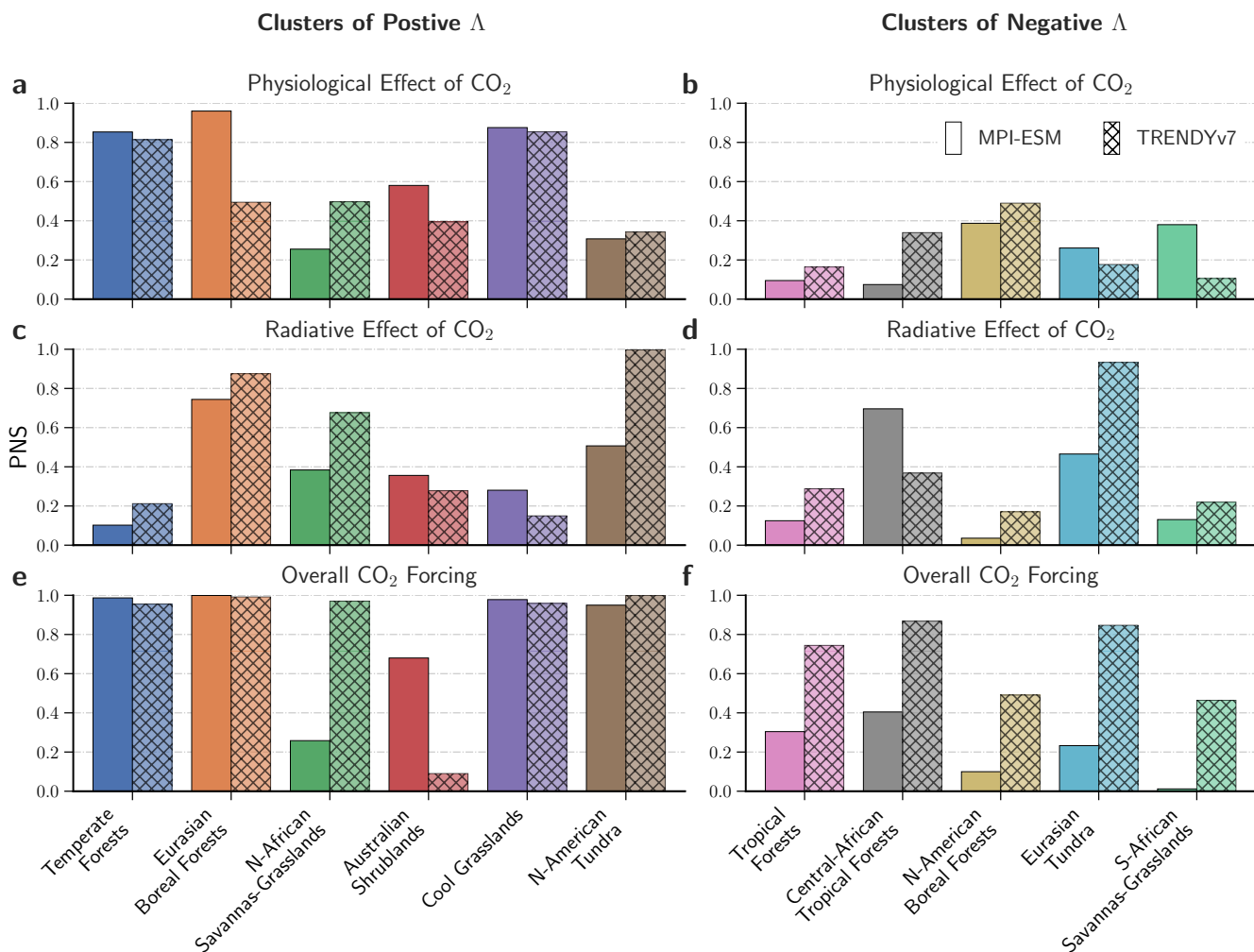
Figure 6. Probabilities of sufficient and necessary causation (PNS) of LAI changes in response to the effects of rising CO₂ for eleven clusters. Bar charts represent PNS of LAI changes in response to the physiological effect (**a, b**), radiative effect of CO₂ (**c, d**) and all anthropogenic forcings (**e, f**). Different colors represent the identified clusters of substantial change in LAI. Panels on the left comprise clusters that show consistent greening, panels on the right represent emerging browning clusters (observed net leaf area loss in the period 2000–2017; attribution is conducted only for significant decreasing trends; see Section 2 for details). The two types of bar illustrate the two different ensembles of model simulations (left: MPI-ESM, right: TRENDYv7).

4   Conclusions

In this paper we examine nearly four decades of global LAI changes under rising atmospheric CO_2 concentration. We find that the Earth's greening trend is weakening and clusters of browning are beginning to emerge, and importantly, expanding during the last two decades. With one exception, all analyzed satellite observation datasets confirm these results, but with different signal strengths. Leaf area is primarily decreasing in the pan-tropical green belt of dense vegetation. Leaf area gain is occurring mostly in sparsely vegetated regions in cold and/or arid climatic zones, and in temperate forests. Thus, vegetation greening is occurring mainly in regions of low LAI, whereas browning is seen primarily in regions of high LAI. Consequently, these opposing trends are decreasing the texture of leaf area distribution in natural vegetation.

We identify clusters of greening and browning spread across all continents and conduct a regional, *i.e.* biome-specific, driver attribution based on factorial model simulations. The results suggest that the physiological effect of CO_2 (*i.e.* CO_2 fertilization) is the dominant driver of increasing leaf area only in temperate forests, cool arid grasslands and likely the Australian shrublands. A cause-and-effect relationship between CO_2 fertilization and greening of other biomes could not be established. This finding questions the study by Zhu et al. (2016) that identified CO_2 fertilization as the globally prevailing driver of the Earth's greening trend. We find that many clusters of greening and browning bear the signature of climatic changes. The greening of Sub-Saharan grasslands and savannas is consistent with increase in rainfall. Climatic changes, primarily warming and drying, determine the patterns of vegetation changes in the northern ecosystems, *i.e.* greening of Eurasian boreal forests and North American tundra, but also emerging browning trend in the Eurasian tundra. Models fail to capture the browning of North American boreal forests. Models suggest rising CO_2 has compensatory effects on LAI in the tropical forests. Climatic changes induce browning, which is opposed by greening due to a strong physiological effect in the models. Hence, if the physiological effect of CO_2 is "turned-off", models simulate the emerging browning trend in the tropics comparable to observations. Our analysis of changes in rainfall during the satellite age underpins climate changes as the main cause of tropical forest browning: recurrent droughts and decline in dry season precipitation in the Amazon as well as long-term drying trends in Africa.

Models represent a simplified view of the real world reduced to its essential processes. Some of these processes are under-represented or lacking in the current generation of land-surface models. Whether they are driven with observed climatic conditions or operate in a fully-coupled Earth system model, they fail to capture the full extent of adverse effects of rising CO_2 in natural ecosystems. In particular, the deficiency of reproducing the observed leaf area loss in North American boreal and in pan-tropical forests – biomes which account for a large part of the photosynthetic carbon fixation – has considerable implications for future climate projections. Thus, it is important to focus model development not only on a better representation of disturbances such as droughts and wildfires, but also on revising the implementation of processes associated with the physiological effect of CO_2, which currently offsets browning induced by climatic changes.

Another vital issue for future research is the impact of large-scale climatic anomalies on vegetation. All three major clusters of browning are hypothesized to be associated with temperature or precipitation anomalies modulated by climatic modes. Many droughts in the Amazon were attributed to El Niño events (Bonal et al., 2016). The long-term drying trend in tropical Africa is possibly connected to the Atlantic Multidecadal Oscillation (Asefi-Najafabady and Saatchi, 2013). Likewise, disturbances

in North American boreal forests are likely controlled by an interplay between large-scale climatic patterns (Pacific Decadal Oscillation, El Niño Southern Oscillation, and Arctic Oscillation; Macias Fauria and Johnson, 2008). Little is known about how these large-scale patterns might change in a warming climate. Current Earth system models struggle to simulate these climatic modes and related precipitation patterns, which is likely rooted in their coarse spatial resolution. New tools, such as high-resolution simulations or large ensembles, offer possibilities to study these phenomena.

Overall, our study suggests that the Earth largely greened in the 1980s and 1990s as rising CO_2 triggered mainly LAI-increasing effects, e.g., by warming the high northern latitudes and overall more carbon allocation through CO_2 fertilization. However, as CO_2 continues to rise, the system appears to be entering or has entered a regime in which LAI-decreasing effects are amplified, i.e., climatic changes associated with rising atmospheric CO_2 concentration become more pronounced and have stronger adverse effects in various ecosystems. In addition, plant sensitivity to CO_2 fertilization may already be saturating, as recently suggested by Wang et al. (2020), but this aspect remains controversial.

We show that the effects of rising CO_2 on LAI are not comparable across the biomes, as are the impacts on the ecosystems. Regarding biodiversity, the consequences of leaf area loss in tropical forests that harbor the most diverse flora and fauna of the planet are not compensated for by leaf area gain in temperate and arctic ecosystems. A similar caveat is in order with respect to the carbon cycle, e.g. an additional leaf in the tundra does not offset the reduction in primary productivity of a leaf lost in the tropical rainforest. Thus, our results indicating loss of tropical leaf area should be of concern. A recent study suggested that the tropical forests have already switched to being a net source of carbon, also considering land-use emissions (Baccini et al., 2017). The uncertainty in future projections is large, ranging from a stable CO_2 fertilization-driven carbon sink to a collapse of the system at a certain CO_2 concentration (Cox et al., 2000). Concerning leaf area, the models project a steady greening of the tropical forests in the high-end CO_2 emissions scenario (business-as-usual) and a slight browning in the low-end scenario (mitigation) by the end of the century (Piao et al., 2019). Altogether, the tropical forests have the potential to crucially influence the evolution of climate throughout the 21st century and should be a vital issue for future research.

Author contributions. A.J.W. performed the research and drafted the manuscript with inputs from R.B.M., V.B., S.S., V.H., D.L, V.K.A.,
690   J.P., J.E.M.S.N., D.S.G., E.K., H.T., A.A., and P.F.; A.J.W. carried out the attribution analysis with support from A.H.; R.B.M., A.H. and V.B. contributed ideas and to the interpretation of the results.

References

Abis, B. and Brovkin, V.: Environmental Conditions for Alternative Tree-Cover States in High Latitudes, Biogeosciences, 14, 511–527, https://doi.org/10.5194/bg-14-511-2017, 2017.

Adler, R. F., Gu, G., Sapiano, M., Wang, J.-J., and Huffman, G. J.: Global Precipitation: Means, Variations and Trends During the Satellite Era (1979–2014), Surveys in Geophysics, 38, 679–699, https://doi.org/10.1007/S10712-017-9416-4, 2017.

Aldrich, S., Walker, R., Simmons, C., Caldas, M., and Perz, S.: Contentious Land Change in the Amazon's Arc of Deforestation, Annals of the Association of American Geographers, 102, 103–128, https://doi.org/10.1080/00045608.2011.620501, 2012.

Anav, A., Friedlingstein, P., Kidston, M., Bopp, L., Ciais, P., Cox, P., Jones, C., Jung, M., Myneni, R., and Zhu, Z.: Evaluating the Land and Ocean Components of the Global Carbon Cycle in the CMIP5 Earth System Models, Journal of Climate, 26, 6801–6843, https://doi.org/10.1175/JCLI-D-12-00417.1, 2013.

Anderson, L. O., Ribeiro Neto, G., Cunha, A. P., Fonseca, M. G., Mendes de Moura, Y., Dalagnol, R., Wagner, F. H., and de Aragão, L. E. O. e. C.: Vulnerability of Amazonian Forests to Repeated Droughts, Philosophical Transactions of the Royal Society B: Biological Sciences, 373, 20170411, https://doi.org/10.1098/rstb.2017.0411, 2018.

Asefi-Najafabady, S. and Saatchi, S.: Response of African Humid Tropical Forests to Recent Rainfall Anomalies, Philosophical Transactions of the Royal Society B: Biological Sciences, 368, 20120306, https://doi.org/10.1098/RSTB.2012.0306, 2013.

Asner, G. P. and Alencar, A.: Drought Impacts on the Amazon Forest: The Remote Sensing Perspective, New Phytologist, pp. 569–578, https://doi.org/10.1111/j.1469-8137.2010.03310.x, 2010.

Baccini, A., Walker, W., Carvalho, L., Farina, M., Sulla-Menashe, D., and Houghton, R. A.: Tropical Forests Are a Net Carbon Source Based on Aboveground Measurements of Gain and Loss, Science, 358, 230–234, https://doi.org/10.1126/science.aam5962, 2017.

Ballantyne, A., Smith, W., Anderegg, W., Kauppi, P., Sarmiento, J., Tans, P., Shevliakova, E., Pan, Y., Poulter, B., Anav, A., Friedlingstein, P., Houghton, R., and Running, S.: Accelerating Net Terrestrial Carbon Uptake during the Warming Hiatus Due to Reduced Respiration, Nature Climate Change, 7, 148–152, https://doi.org/10.1038/nclimate3204, 2017.

Bastos, A., Friedlingstein, P., Sitch, S., Chen, C., Mialon, A., Wigneron, J.-P., Arora, V. K., Briggs, P. R., Canadell, J. G., Ciais, P., Chevallier, F., Cheng, L., Delire, C., Haverd, V., Jain, A. K., Joos, F., Kato, E., Lienert, S., Lombardozzi, D., Melton, J. R., Myneni, R., Nabel, J. E. M. S., Pongratz, J., Poulter, B., Rödenbeck, C., Séférian, R., Tian, H., van Eck, C., Viovy, N., Vuichard, N., Walker, A. P., Wiltshire, A., Yang, J., Zaehle, S., Zeng, N., and Zhu, D.: Impact of the 2015/2016 El Niño on the Terrestrial Carbon Cycle Constrained by Bottom-up and Top-down Approaches, Phil. Trans. R. Soc. B, 373, 20170304, https://doi.org/10.1098/rstb.2017.0304, 2018.

Bastos, A., Ciais, P., Chevallier, F., Rödenbeck, C., Ballantyne, A. P., Maignan, F., Yin, Y., Fernández-Martínez, M., Friedlingstein, P., Peñuelas, J., Piao, S. L., Sitch, S., Smith, W. K., Wang, X., Zhu, Z., Haverd, V., Kato, E., Jain, A. K., Lienert, S., Lombardozzi, D., Nabel, J. E. M. S., Peylin, P., Poulter, B., and Zhu, D.: Contrasting Effects of CO_2 Fertilization, Land-Use Change and Warming on Seasonal Amplitude of Northern Hemisphere CO_2 Exchange, Atmospheric Chemistry and Physics, 19, 12361–12375, https://doi.org/10.5194/acp-19-12361-2019, 2019.

Beck, P. S. A. and Goetz, S. J.: Satellite Observations of High Northern Latitude Vegetation Productivity Changes between 1982 and 2008: Ecological Variability and Regional Differences, Environmental Research Letters, 6, 045501, https://doi.org/10.1088/1748-9326/6/4/045501, 2011.

Bhatt, U. S., Walker, D. A., Raynolds, M. K., Bieniek, P. A., Epstein, H. E., Comiso, J. C., Pinzon, J. E., Tucker, C. J., and Polyakov, I. V.: Recent Declines in Warming and Vegetation Greening Trends over Pan-Arctic Tundra, Remote Sensing, 5, 4229–4254, https://doi.org/10.3390/rs5094229, 2013.

Bhatt, U. S., Walker, D. A., Walsh, J. E., Carmack, E. C., Frey, K. E., Meier, W. N., Moore, S. E., Parmentier, F.-J. W., Post, E., Romanovsky, V. E., and Simpson, W. R.: Implications of Arctic Sea Ice Decline for the Earth System, Annual Review of Environment and Resources, 39, 57–89, https://doi.org/10.1146/annurev-environ-122012-094357, 2014.

Bonal, D., Burban, B., Stahl, C., Wagner, F., and Hérault, B.: The Response of Tropical Rainforests to Drought—Lessons from Recent Research and Future Prospects, Annals of Forest Science, 73, 27–44, https://doi.org/10.1007/S13595-015-0522-5, 2016.

Bonan, G. B.: Forests and Climate Change: Forcings, Feedbacks, and the Climate Benefits of Forests, Science, 320, 1444–1449, https://doi.org/10.1126/science.1155121, 2008.

Cai, W., Borlace, S., Lengaigne, M., van Rensch, P., Collins, M., Vecchi, G., Timmermann, A., Santoso, A., McPhaden, M. J., Wu, L., England, M. H., Wang, G., Guilyardi, E., and Jin, F.-F.: Increasing Frequency of Extreme El Niño Events Due to Greenhouse Warming, Nature Climate Change, 4, 111–116, https://doi.org/10.1038/NCLIMATE2100, 2014.

Chen, C., Park, T., Wang, X., Piao, S., Xu, B., Chaturvedi, R. K., Fuchs, R., Brovkin, V., Ciais, P., Fensholt, R., Tømmervik, H., Bala, G., Zhu, Z., Nemani, R. R., and Myneni, R. B.: China and India Lead in Greening of the World through Land-Use Management, Nature Sustainability, 2, 122, https://doi.org/10.1038/s41893-019-0220-7, 2019.

Claverie, M., Matthews, J. L., Vermote, E. F., and Justice, C. O.: A 30+ Year AVHRR LAI and FAPAR Climate Data Record: Algorithm Description and Validation, Remote Sensing, 8, 263, https://doi.org/10.3390/rs8030263, 2016.

Cox, P. M., Betts, R. A., Jones, C. D., Spall, S. A., and Totterdell, I. J.: Acceleration of Global Warming Due to Carbon-Cycle Feedbacks in a Coupled Climate Model, Nature, 408, 184–187, https://doi.org/10.1038/35041539, 2000.

Currie, W. S. and Bergen, K. M.: Temperate Forest, in: Encyclopedia of Ecology, edited by Jørgensen, S. E. and Fath, B. D., pp. 3494–3503, Academic Press, Oxford, UK, https://doi.org/10.1016/B978-008045405-4.00704-7, 2008.

Dee, D. P., Uppala, S. M., Simmons, A. J., Berrisford, P., Poli, P., Kobayashi, S., Andrae, U., Balmaseda, M. A., Balsamo, G., Bauer, P., Bechtold, P., Beljaars, A. C. M., van de Berg, L., Bidlot, J., Bormann, N., Delsol, C., Dragani, R., Fuentes, M., Geer, A. J., Haimberger, L., Healy, S. B., Hersbach, H., Hólm, E. V., Isaksen, L., Kållberg, P., Köhler, M., Matricardi, M., McNally, A. P., Monge-Sanz, B. M., Morcrette, J.-J., Park, B.-K., Peubey, C., de Rosnay, P., Tavolato, C., Thépaut, J.-N., and Vitart, F.: The ERA-Interim Reanalysis: Configuration and Performance of the Data Assimilation System, Quarterly Journal of the Royal Meteorological Society, 137, 553–597, https://doi.org/10.1002/qj.828, 2011.

Donohue, R. J., McVicar, T. R., and Roderick, M. L.: Climate-Related Trends in Australian Vegetation Cover as Inferred from Satellite Observations, 1981–2006, Global Change Biology, 15, 1025–1039, https://doi.org/10.1111/J.1365-2486.2008.01746.X, 2009.

Donohue, R. J., Roderick, M. L., McVicar, T. R., and Farquhar, G. D.: Impact of CO2 Fertilization on Maximum Foliage Cover across the Globe's Warm, Arid Environments, Geophysical Research Letters, 40, 3031–3035, https://doi.org/10.1002/GRL.50563, 2013.

Eyring, V., Bony, S., Meehl, G. A., Senior, C. A., Stevens, B., Stouffer, R. J., and Taylor, K. E.: Overview of the Coupled Model Intercomparison Project Phase 6 (CMIP6) Experimental Design and Organization, Geoscientific Model Development, 9, 1937–1958, https://doi.org/10.5194/gmd-9-1937-2016, 2016.

Fasullo, J. T., Otto-Bliesner, B. L., and Stevenson, S.: ENSO's Changing Influence on Temperature, Precipitation, and Wildfire in a Warming Climate, Geophysical Research Letters, 45, 9216–9225, https://doi.org/10.1029/2018GL079022, 2018.

Fatichi, S., Leuzinger, S., Paschalis, A., Langley, J. A., Barraclough, A. D., and Hovenden, M. J.: Partitioning Direct and Indirect Effects Reveals the Response of Water-Limited Ecosystems to Elevated CO2, Proceedings of the National Academy of Sciences, 113, 12 757–12 762, https://doi.org/10.1073/pnas.1605036113, 2016.

Fensholt, R. and Rasmussen, K.: Analysis of Trends in the Sahelian 'Rain-Use Efficiency' Using GIMMS NDVI, RFE and GPCP Rainfall Data, Remote Sensing of Environment, 115, 438–451, https://doi.org/10.1016/J.RSE.2010.09.014, 2011.

Fensholt, R., Langanke, T., Rasmussen, K., Reenberg, A., Prince, S. D., Tucker, C., Scholes, R. J., Le, Q. B., Bondeau, A., Eastman, R., Epstein, H., Gaughan, A. E., Hellden, U., Mbow, C., Olsson, L., Paruelo, J., Schweitzer, C., Seaquist, J., and Wessels, K.: Greenness in Semi-Arid Areas across the Globe 1981–2007 — an Earth Observing Satellite Based Analysis of Trends and Drivers, Remote Sensing of Environment, 121, 144–158, https://doi.org/10.1016/j.rse.2012.01.017, 2012.

Fernández-Martínez, M., Sardans, J., Chevallier, F., Ciais, P., Obersteiner, M., Vicca, S., Canadell, J. G., Bastos, A., Friedlingstein, P., Sitch, S., Piao, S. L., Janssens, I. A., and Peñuelas, J.: Global Trends in Carbon Sinks and Their Relationships with CO2 and Temperature, Nature Climate Change, 9, 73, https://doi.org/10.1038/s41558-018-0367-7, 2019.

Forkel, M., Carvalhais, N., Rödenbeck, C., Keeling, R., Heimann, M., Thonicke, K., Zaehle, S., and Reichstein, M.: Enhanced Seasonal CO2 Exchange Caused by Amplified Plant Productivity in Northern Ecosystems, Science, 351, 696–699, https://doi.org/10.1126/science.aac4971, 2016.

Forzieri, G., Alkama, R., Miralles, D. G., and Cescatti, A.: Satellites Reveal Contrasting Responses of Regional Climate to the Widespread Greening of Earth, Science, 356, 1180–1184, https://doi.org/10.1126/science.aal1727, 2017.

Fu, R., Yin, L., Li, W., Arias, P. A., Dickinson, R. E., Huang, L., Chakraborty, S., Fernandes, K., Liebmann, B., Fisher, R., and Myneni, R. B.: Increased Dry-Season Length over Southern Amazonia in Recent Decades and Its Implication for Future Climate Projection, Proceedings of the National Academy of Sciences, 110, 18 110–18 115, https://doi.org/10.1073/pnas.1302584110, 2013.

Giorgetta, M. A., Jungclaus, J., Reick, C. H., Legutke, S., Bader, J., Böttinger, M., Brovkin, V., Crueger, T., Esch, M., Fieg, K., Glushak, K., Gayler, V., Haak, H., Hollweg, H.-D., Ilyina, T., Kinne, S., Kornblueh, L., Matei, D., Mauritsen, T., Mikolajewicz, U., Mueller, W., Notz, D., Pithan, F., Raddatz, T., Rast, S., Redler, R., Roeckner, E., Schmidt, H., Schnur, R., Segschneider, J., Six, K. D., Stockhause, M., Timmreck, C., Wegner, J., Widmann, H., Wieners, K.-H., Claussen, M., Marotzke, J., and Stevens, B.: Climate and Carbon Cycle Changes from 1850 to 2100 in MPI-ESM Simulations for the Coupled Model Intercomparison Project Phase 5, Journal of Advances in Modeling Earth Systems, 5, 572–597, https://doi.org/10.1002/jame.20038, 2013.

Goetz, S. J., Bunn, A. G., Fiske, G. J., and Houghton, R. A.: Satellite-Observed Photosynthetic Trends across Boreal North America Associated with Climate and Fire Disturbance, Proceedings of the National Academy of Sciences of the United States of America, 102, 13 521–13 525, https://doi.org/10.1073/pnas.0506179102, 2005.

Gu, G., Adler, R. F., and Huffman, G. J.: Long-Term Changes/Trends in Surface Temperature and Precipitation during the Satellite Era (1979–2012), Climate Dynamics, 46, 1091–1105, https://doi.org/10.1007/S00382-015-2634-X, 2016.

Hannart, A. and Naveau, P.: Probabilities of Causation of Climate Changes, Journal of Climate, 31, 5507–5524, https://doi.org/10.1175/JCLI-D-17-0304.1, 2018.

Hannart, A., Pearl, J., Otto, F. E. L., Naveau, P., and Ghil, M.: Causal Counterfactual Theory for the Attribution of Weather and Climate-Related Events, Bulletin of the American Meteorological Society, 97, 99–110, https://doi.org/10.1175/BAMS-D-14-00034.1, 2016.

Harris, I., Jones, P. D., Osborn, T. J., and Lister, D. H.: Updated High-Resolution Grids of Monthly Climatic Observations – the CRU TS3.10 Dataset, International Journal of Climatology, 34, 623–642, https://doi.org/10.1002/joc.3711, 2014.

810   Hedemann, C., Mauritsen, T., Jungclaus, J., and Marotzke, J.: The Subtle Origins of Surface-Warming Hiatuses, Nature Climate Change, 7, 336–339, https://doi.org/10.1038/nclimate3274, 2017.

Hurtt, G. C., Chini, L. P., Frolking, S., Betts, R. A., Feddema, J., Fischer, G., Fisk, J. P., Hibbard, K., Houghton, R. A., Janetos, A., Jones, C. D., Kindermann, G., Kinoshita, T., Klein Goldewijk, K., Riahi, K., Shevliakova, E., Smith, S., Stehfest, E., Thomson, A., Thornton, P., van Vuuren, D. P., and Wang, Y. P.: Harmonization of Land-Use Scenarios for the Period 1500–2100: 600 Years of Global Gridded Annual
815   Land-Use Transitions, Wood Harvest, and Resulting Secondary Lands, Climatic Change, 109, 117, https://doi.org/10.1007/S10584-011-0153-2, 2011.

Jiménez-Muñoz, J. C., Mattar, C., Barichivich, J., Santamaría-Artigas, A., Takahashi, K., Malhi, Y., Sobrino, J. A., and van der Schrier, G.: Record-Breaking Warming and Extreme Drought in the Amazon Rainforest during the Course of El Niño 2015–2016, Scientific Reports, 6, 33 130, https://doi.org/10.1038/SREP33130, 2016.

820   Jones, P. W.: First- and Second-Order Conservative Remapping Schemes for Grids in Spherical Coordinates, Monthly Weather Review, 127, 2204–2210, https://doi.org/10.1175/1520-0493(1999)127<2204:FASOCR>2.0.CO;2, 1999.

Keenan, T. F., Prentice, I. C., Canadell, J. G., Williams, C. A., Wang, H., Raupach, M., and Collatz, G. J.: Recent Pause in the Growth Rate of Atmospheric CO2 Due to Enhanced Terrestrial Carbon Uptake, Nature Communications, 7, 13 428, https://doi.org/10.1038/ncomms13428, 2016.

825   Kolby Smith, W., Reed, S. C., Cleveland, C. C., Ballantyne, A. P., Anderegg, W. R. L., Wieder, W. R., Liu, Y. Y., and Running, S. W.: Large Divergence of Satellite and Earth System Model Estimates of Global Terrestrial CO2 Fertilization, Nature Climate Change, 6, 306–310, https://doi.org/10.1038/nclimate2879, 2016.

Kurz, W. A., Stinson, G., Rampley, G. J., Dymond, C. C., and Neilson, E. T.: Risk of Natural Disturbances Makes Future Contribution of Canada's Forests to the Global Carbon Cycle Highly Uncertain, Proceedings of the National Academy of Sciences, 105, 1551–1555,
830   https://doi.org/10.1073/pnas.0708133105, 2008.

Lammertsma, E. I., de Boer, H. J., Dekker, S. C., Dilcher, D. L., Lotter, A. F., and Wagner-Cremer, F.: Global CO2 Rise Leads to Reduced Maximum Stomatal Conductance in Florida Vegetation, Proceedings of the National Academy of Sciences, 108, 4035–4040, https://doi.org/10.1073/pnas.1100371108, 2011.

Langenbrunner, B., Pritchard, M. S., Kooperman, G. J., and Randerson, J. T.: Why Does Amazon Precipitation Decrease When Tropical
835   Forests Respond to Increasing CO2?, Earth's Future, 7, 450–468, https://doi.org/10.1029/2018EF001026, 2019.

Leakey, A. D. B., Ainsworth, E. A., Bernacchi, C. J., Rogers, A., Long, S. P., and Ort, D. R.: Elevated CO2 Effects on Plant Carbon, Nitrogen, and Water Relations: Six Important Lessons from FACE, Journal of Experimental Botany, 60, 2859–2876, https://doi.org/10.1093/jxb/erp096, 2009.

Liu, Y., Liu, R., and Chen, J. M.: Retrospective Retrieval of Long-Term Consistent Global Leaf Area Index (1981–2011) from Combined
840   AVHRR and MODIS Data, Journal of Geophysical Research: Biogeosciences, 117, G04 003, https://doi.org/10.1029/2012JG002084, 2012.

Lucht, W., Prentice, I. C., Myneni, R. B., Sitch, S., Friedlingstein, P., Cramer, W., Bousquet, P., Buermann, W., and Smith, B.: Climatic Control of the High-Latitude Vegetation Greening Trend and Pinatubo Effect, Science, 296, 1687, https://doi.org/10.1126/science.1071828, 2002.

845   MacDicken, K., Jonsson, Ö., Piña, L., Maulo, S., Contessa, V., Adikari, Y., Garzuglia, M., Lindquist, E., Reams, G., and D'Annunzio, R.: Global Forest Resources Assessment 2015: How Are the World's Forests Changing?, Food and Agriculture Organization of the United Nations, Rome, 2015.

Macias Fauria, M. and Johnson, E.: Climate and Wildfires in the North American Boreal Forest, Philosophical Transactions of the Royal Society B: Biological Sciences, 363, 2317–2329, https://doi.org/10.1098/RSTB.2007.2202, 2008.

850   Maeda, E. E., Kim, H., Aragão, L. E. O. C., Famiglietti, J. S., and Oki, T.: Disruption of Hydroecological Equilibrium in Southwest Amazon Mediated by Drought, Geophysical Research Letters, 42, 7546–7553, https://doi.org/10.1002/2015GL065252, 2015.

Mahowald, N., Lo, F., Zheng, Y., Harrison, L., Funk, C., Lombardozzi, D., and Goodale, C.: Projections of Leaf Area Index in Earth System Models, Earth Syst. Dynam., 7, 211–229, https://doi.org/10.5194/esd-7-211-2016, 2016.

Malhi, Y. and Wright, J.: Spatial Patterns and Recent Trends in the Climate of Tropical Rainforest Regions, Philosophical Transactions of

855   the Royal Society of London. Series B: Biological Sciences, 359, 311–329, https://doi.org/10.1098/RSTB.2003.1433, 2004.

Mao, J., Ribes, A., Yan, B., Shi, X., Thornton, P. E., Séférian, R., Ciais, P., Myneni, R. B., Douville, H., Piao, S., Zhu, Z., Dickinson, R. E., Dai, Y., Ricciuto, D. M., Jin, M., Hoffman, F. M., Wang, B., Huang, M., and Lian, X.: Human-Induced Greening of the Northern Extratropical Land Surface, Nature Climate Change, 6, 959–963, https://doi.org/10.1038/nclimate3056, 2016.

Marengo, J. A., Nobre, C. A., Tomasella, J., Oyama, M. D., Sampaio de Oliveira, G., de Oliveira, R., Camargo, H., Alves, L. M., and Brown,

860   I. F.: The Drought of Amazonia in 2005, Journal of Climate, 21, 495–516, https://doi.org/10.1175/2007JCLI1600.1, 2008.

Marengo, J. A., Tomasella, J., Alves, L. M., Soares, W. R., and Rodriguez, D. A.: The Drought of 2010 in the Context of Historical Droughts in the Amazon Region, Geophysical Research Letters, 38, https://doi.org/10.1029/2011GL047436, 2011.

Marotzke, J.: Quantifying the Irreducible Uncertainty in Near-term Climate Projections, Wiley Interdisciplinary Reviews: Climate Change, 10, e563, https://doi.org/10.1002/wcc.563, 2019.

865   Marotzke, J., Jakob, C., Bony, S., Dirmeyer, P. A., O'Gorman, P. A., Hawkins, E., Perkins-Kirkpatrick, S., Quéré, C. L., Nowicki, S., Paulavets, K., Seneviratne, S. I., Stevens, B., and Tuma, M.: Climate Research Must Sharpen Its View, Nature Climate Change, 7, 89–91, https://doi.org/10.1038/nclimate3206, 2017.

Mastrandrea, M. D., Mach, K. J., Plattner, G.-K., Edenhofer, O., Stocker, T. F., Field, C. B., Ebi, K. L., and Matschoss, P. R.: The IPCC AR5 Guidance Note on Consistent Treatment of Uncertainties: A Common Approach across the Working Groups, Climatic Change, 108, 675,

870   https://doi.org/10.1007/S10584-011-0178-6, 2011.

Mauritsen, T., Bader, J., Becker, T., Behrens, J., Bittner, M., Brokopf, R., Brovkin, V., Claussen, M., Crueger, T., Esch, M., Fast, I., Fiedler, S., Fläschner, D., Gayler, V., Giorgetta, M., Goll, D. S., Haak, H., Hagemann, S., Hedemann, C., Hohenegger, C., Ilyina, T., Jahns, T., Jimenéz-de-la Cuesta, D., Jungclaus, J., Kleinen, T., Kloster, S., Kracher, D., Kinne, S., Kleberg, D., Lasslop, G., Kornblueh, L., Marotzke, J., Matei, D., Meraner, K., Mikolajewicz, U., Modali, K., Möbis, B., Müller, W. A., Nabel, J. E. M. S., Nam, C. C. W., Notz,

875   D., Nyawira, S.-S., Paulsen, H., Peters, K., Pincus, R., Pohlmann, H., Pongratz, J., Popp, M., Raddatz, T. J., Rast, S., Redler, R., Reick, C. H., Rohrschneider, T., Schemann, V., Schmidt, H., Schnur, R., Schulzweida, U., Six, K. D., Stein, L., Stemmler, I., Stevens, B., von Storch, J.-S., Tian, F., Voigt, A., Vrese, P., Wieners, K.-H., Wilkenskjeld, S., Winkler, A., and Roeckner, E.: Developments in the MPI-M Earth System Model Version 1.2 (MPI-ESM1.2) and Its Response to Increasing CO2, Journal of Advances in Modeling Earth Systems, 11, 998–1038, https://doi.org/10.1029/2018MS001400, 2019.

880   Mayaux, P., Pekel, J.-F., Baudouin, D., Donnay, F., Achard, F., Clerici, M., Bodart, C., Brink, A., Nasi, R., and Belward, A.: State and Evolution of the African Rainforests between 1990 and 2010, Philosophical Transactions of the Royal Society B: Biological Sciences, 368, 20120 300, https://doi.org/10.1098/rstb.2012.0300, 2013.

McPherson, R. A.: A Review of Vegetation—Atmosphere Interactions and Their Influences on Mesoscale Phenomena, Progress in Physical Geography: Earth and Environment, 31, 261–285, https://doi.org/10.1177/0309133307079055, 2007.

885 Munday, C. and Washington, R.: Controls on the Diversity in Climate Model Projections of Early Summer Drying over Southern Africa, Journal of Climate, 32, 3707–3725, https://doi.org/10.1175/JCLI-D-18-0463.1, 2019.

Murray-Tortarolo, G., Anav, A., Friedlingstein, P., Sitch, S., Piao, S., Zhu, Z., Poulter, B., Zaehle, S., Ahlström, A., Lomas, M., Levis, S., Viovy, N., and Zeng, N.: Evaluation of Land Surface Models in Reproducing Satellite-Derived LAI over the High-Latitude Northern Hemisphere. Part I: Uncoupled DGVMs, Remote Sensing, 5, 4819–4838, https://doi.org/10.3390/RS5104819, 2013.

890 Myneni, R. B., Keeling, C. D., Tucker, C. J., Asrar, G., and Nemani, R. R.: Increased Plant Growth in the Northern High Latitudes from 1981 to 1991, Nature, 386, 698–702, https://doi.org/10.1038/386698a0, 1997.

Myneni, R. B., Knyazikhin, Y., and Park, T.: MOD15A2H MODIS/Terra Leaf Area Index/FPAR 8-Day L4 Global 500m SIN Grid V006, 2015a.

Myneni, R. B., Knyazikhin, Y., and Park, T.: MYD15A2H MODIS/Aqua Leaf Area Index/FPAR 8-Day L4 Global 500m SIN Grid V006, 895 2015b.

Nemani, R. R., Keeling, C. D., Hashimoto, H., Jolly, W. M., Piper, S. C., Tucker, C. J., Myneni, R. B., and Running, S. W.: Climate-Driven Increases in Global Terrestrial Net Primary Production from 1982 to 1999, Science, 300, 1560–1563, https://doi.org/10.1126/science.1082750, 2003.

Park, C.-E., Jeong, S.-J., Joshi, M., Osborn, T. J., Ho, C.-H., Piao, S., Chen, D., Liu, J., Yang, H., Park, H., Kim, B.-M., and 900 Feng, S.: Keeping Global Warming within 1.5 $\circ$C Constrains Emergence of Aridification, Nature Climate Change, 8, 70, https://doi.org/10.1038/S41558-017-0034-4, 2018.

Park, T., Ganguly, S., Tømmervik, H., Euskirchen, E. S., Høgda, K.-A., Karlsen, S. R., Brovkin, V., Nemani, R. R., and Myneni, R. B.: Changes in Growing Season Duration and Productivity of Northern Vegetation Inferred from Long-Term Remote Sensing Data, Environmental Research Letters, 11, 084 001, https://doi.org/10.1088/1748-9326/11/8/084001, 2016.

905 Pearl, J.: Causality: Models, Reasoning and Inference, Cambridge University Press, Cambridge, second edn., https://doi.org/10.1017/CBO9780511803161, 2009.

Pedelty, J., Devadiga, S., Masuoka, E., Brown, M., Pinzon, J., Tucker, C., Vermote, E., Prince, S., Nagol, J., Justice, C., Roy, D., Junchang Ju, Schaaf, C., Jicheng Liu, Privette, J., and Pinheiro, A.: Generating a Long-Term Land Data Record from the AVHRR and MODIS Instruments, in: 2007 IEEE International Geoscience and Remote Sensing Symposium, pp. 1021–1025, 910 https://doi.org/10.1109/IGARSS.2007.4422974, 2007.

Phoenix, G. K. and Bjerke, J. W.: Arctic Browning: Extreme Events and Trends Reversing Arctic Greening, Global Change Biology, 22, 2960–2962, https://doi.org/10.1111/GCB.13261, 2016.

Piao, S., Wang, X., Ciais, P., Zhu, B., Wang, T., and Liu, J.: Changes in Satellite-Derived Vegetation Growth Trend in Temperate and Boreal Eurasia from 1982 to 2006, Global Change Biology, 17, 3228–3239, https://doi.org/10.1111/J.1365-2486.2011.02419.X, 2011.

915 Piao, S., Nan, H., Huntingford, C., Ciais, P., Friedlingstein, P., Sitch, S., Peng, S., Ahlström, A., Canadell, J. G., Cong, N., Levis, S., Levy, P. E., Liu, L., Lomas, M. R., Mao, J., Myneni, R. B., Peylin, P., Poulter, B., Shi, X., Yin, G., Viovy, N., Wang, T., Wang, X., Zaehle, S., Zeng, N., Zeng, Z., and Chen, A.: Evidence for a Weakening Relationship between Interannual Temperature Variability and Northern Vegetation Activity, Nature Communications, 5, 5018, https://doi.org/10.1038/ncomms6018, 2014.

Piao, S., Wang, X., Park, T., Chen, C., Lian, X., He, Y., Bjerke, J. W., Chen, A., Ciais, P., Tømmervik, H., Nemani, R. R., and 920 Myneni, R. B.: Characteristics, Drivers and Feedbacks of Global Greening, Nature Reviews Earth & Environment, pp. 1–14, https://doi.org/10.1038/s43017-019-0001-x, 2019.

Pinzon, J. E. and Tucker, C. J.: A Non-Stationary 1981–2012 AVHRR NDVI3g Time Series, Remote Sensing, 6, 6929–6960, https://doi.org/10.3390/rs6086929, 2014.

Poulter, B., Frank, D., Ciais, P., Myneni, R. B., Andela, N., Bi, J., Broquet, G., Canadell, J. G., Chevallier, F., Liu, Y. Y., Running, S. W.,
925   Sitch, S., and van der Werf, G. R.: Contribution of Semi-Arid Ecosystems to Interannual Variability of the Global Carbon Cycle, Nature, 509, 600–603, https://doi.org/10.1038/nature13376, 2014.

Pugh, T. A. M., Lindeskog, M., Smith, B., Poulter, B., Arneth, A., Haverd, V., and Calle, L.: Role of Forest Regrowth in Global Carbon Sink Dynamics, Proceedings of the National Academy of Sciences, 116, 4382–4387, https://doi.org/10.1073/pnas.1810512116, 2019.

Quéré, C. L., Andrew, R. M., Friedlingstein, P., Sitch, S., Hauck, J., Pongratz, J., Pickers, P. A., Korsbakken, J. I., Peters, G. P., Canadell,
930   J. G., Arneth, A., Arora, V. K., Barbero, L., Bastos, A., Bopp, L., Chevallier, F., Chini, L. P., Ciais, P., Doney, S. C., Gkritzalis, T., Goll, D. S., Harris, I., Haverd, V., Hoffman, F. M., Hoppema, M., Houghton, R. A., Hurtt, G., Ilyina, T., Jain, A. K., Johannessen, T., Jones, C. D., Kato, E., Keeling, R. F., Goldewijk, K. K., Landschützer, P., Lefèvre, N., Lienert, S., Liu, Z., Lombardozzi, D., Metzl, N., Munro, D. R., Nabel, J. E. M. S., Nakaoka, S.-i., Neill, C., Olsen, A., Ono, T., Patra, P., Peregon, A., Peters, W., Peylin, P., Pfeil, B., Pierrot, D., Poulter, B., Rehder, G., Resplandy, L., Robertson, E., Rocher, M., Rödenbeck, C., Schuster, U., Schwinger, J., Séférian, R., Skjelvan,
935   I., Steinhoff, T., Sutton, A., Tans, P. P., Tian, H., Tilbrook, B., Tubiello, F. N., van der Laan-Luijkx, I. T., van der Werf, G. R., Viovy, N., Walker, A. P., Wiltshire, A. J., Wright, R., Zaehle, S., and Zheng, B.: Global Carbon Budget 2018, Earth System Science Data, 10, 2141–2194, https://doi.org/10.5194/ESSD-10-2141-2018, 2018.

Rodell, M., Houser, P. R., Jambor, U., Gottschalck, J., Mitchell, K., Meng, C.-J., Arsenault, K., Cosgrove, B., Radakovich, J., Bosilovich, M., Entin, J. K., Walker, J. P., Lohmann, D., and Toll, D.: The Global Land Data Assimilation System, Bulletin of the American Meteorological
940   Society, 85, 381–394, https://doi.org/10.1175/BAMS-85-3-381, 2004.

Saatchi, S., Asefi-Najafabady, S., Malhi, Y., Aragão, L. E. O. C., Anderson, L. O., Myneni, R. B., and Nemani, R.: Persistent Effects of a Severe Drought on Amazonian Forest Canopy, Proceedings of the National Academy of Sciences, 110, 565–570, https://doi.org/10.1073/PNAS.1204651110, 2013.

Sachs, L.: Angewandte Statistik, Springer Berlin Heidelberg, https://doi.org/10.1007/978-3-662-05746-9, 1997.

945   Sage, R. F., Sage, T. L., and Ocarina, F.: Photorespiration and the Evolution of C4 Photosynthesis, Annual Review of Plant Biology, 63, 19–47, https://doi.org/10.1146/ANNUREV-ARPLANT-042811-105511, 2012.

Seidl, R., Thom, D., Kautz, M., Martin-Benito, D., Peltoniemi, M., Vacchiano, G., Wild, J., Ascoli, D., Petr, M., Honkaniemi, J., Lexer, M. J., Trotsiuk, V., Mairota, P., Svoboda, M., Fabrika, M., Nagel, T. A., and Reyer, C. P. O.: Forest Disturbances under Climate Change, Nature Climate Change, 7, 395–402, https://doi.org/10.1038/NCLIMATE3303, 2017.

950   Sitch, S., Friedlingstein, P., Gruber, N., Jones, S. D., Murray-Tortarolo, G., Ahlström, A., Doney, S. C., Graven, H., Heinze, C., Huntingford, C., Levis, S., Levy, P. E., Lomas, M., Poulter, B., Viovy, N., Zaehle, S., Zeng, N., Arneth, A., Bonan, G., Bopp, L., Canadell, J. G., Chevallier, F., Ciais, P., Ellis, R., Gloor, M., Peylin, P., Piao, S. L., Le Quéré, C., Smith, B., Zhu, Z., and Myneni, R.: Recent Trends and Drivers of Regional Sources and Sinks of Carbon Dioxide, Biogeosciences, 12, 653–679, https://doi.org/10.5194/BG-12-653-2015, 2015.

Song, X.-P., Huang, C., Saatchi, S. S., Hansen, M. C., and Townshend, J. R.: Annual Carbon Emissions from Deforestation in the Amazon
955   Basin between 2000 and 2010, PLOS ONE, 10, e0126 754, https://doi.org/10.1371/JOURNAL.PONE.0126754, 2015.

Song, X.-P., Hansen, M. C., Stehman, S. V., Potapov, P. V., Tyukavina, A., Vermote, E. F., and Townshend, J. R.: Global Land Change from 1982 to 2016, Nature, p. 1, https://doi.org/10.1038/s41586-018-0411-9, 2018.

Stibig, H.-J., Achard, F., Carboni, S., Raši, R., and Miettinen, J.: Change in Tropical Forest Cover of Southeast Asia from 1990 to 2010, Biogeosciences, 11, 247–258, https://doi.org/10.5194/BG-11-247-2014, 2014.

Still, C. J., Berry, J. A., Collatz, G. J., and DeFries, R. S.: Global Distribution of C3 and C4 Vegetation: Carbon Cycle Implications, Global Biogeochemical Cycles, 17, 6–1–6–14, https://doi.org/10.1029/2001GB001807, 2003.

Thomas, R. T., Prentice, I. C., Graven, H., Ciais, P., Fisher, J. B., Hayes, D. J., Huang, M., Huntzinger, D. N., Ito, A., Jain, A., Mao, J., Michalak, A. M., Peng, S., Poulter, B., Ricciuto, D. M., Shi, X., Schwalm, C., Tian, H., and Zeng, N.: Increased Light-Use Efficiency in Northern Terrestrial Ecosystems Indicated by CO2 and Greening Observations, Geophysical Research Letters, 43, 11,339–11,349, https://doi.org/10.1002/2016GL070710, 2016.

Tyukavina, A., Hansen, M. C., Potapov, P., Parker, D., Okpa, C., Stehman, S. V., Kommareddy, I., and Turubanova, S.: Congo Basin Forest Loss Dominated by Increasing Smallholder Clearing, Science Advances, 4, eaat2993, https://doi.org/10.1126/SCIADV.AAT2993, 2018.

Ukkola, A. M., Prentice, I. C., Keenan, T. F., van Dijk, A. I. J. M., Viney, N. R., Myneni, R. B., and Bi, J.: Reduced Streamflow in Water-Stressed Climates Consistent with CO_2 Effects on Vegetation, Nature Climate Change, 6, 75–78, https://doi.org/10.1038/nclimate2831, 2016.

Verbyla, D.: Browning Boreal Forests of Western North America, Environmental Research Letters, 6, 041 003, https://doi.org/10.1088/1748-9326/6/4/041003, 2011.

Walker, A. P., Kauwe, M. G. D., Bastos, A., Belmecheri, S., Georgiou, K., Keeling, R. F., McMahon, S. M., Medlyn, B. E., Moore, D. J. P., Norby, R. J., Zaehle, S., Anderson-Teixeira, K. J., Battipaglia, G., Brienen, R. J. W., Cabugao, K. G., Cailleret, M., Campbell, E., Canadell, J. G., Ciais, P., Craig, M. E., Ellsworth, D. S., Farquhar, G. D., Fatichi, S., Fisher, J. B., Frank, D. C., Graven, H., Gu, L., Haverd, V., Heilman, K., Heimann, M., Hungate, B. A., Iversen, C. M., Joos, F., Jiang, M., Keenan, T. F., Knauer, J., Körner, C., Leshyk, V. O., Leuzinger, S., Liu, Y., MacBean, N., Malhi, Y., McVicar, T. R., Penuelas, J., Pongratz, J., Powell, A. S., Riutta, T., Sabot, M. E. B., Schleucher, J., Sitch, S., Smith, W. K., Sulman, B., Taylor, B., Terrer, C., Torn, M. S., Treseder, K. K., Trugman, A. T., Trumbore, S. E., van Mantgem, P. J., Voelker, S. L., Whelan, M. E., and Zuidema, P. A.: Integrating the Evidence for a Terrestrial Carbon Sink Caused by Increasing Atmospheric CO2, New Phytologist, 229, 2413–2445, https://doi.org/10.1111/nph.16866, 2021.

Wang, S., Zhang, Y., Ju, W., Chen, J. M., Ciais, P., Cescatti, A., Sardans, J., Janssens, I. A., Wu, M., Berry, J. A., Campbell, E., Fernández-Martínez, M., Alkama, R., Sitch, S., Friedlingstein, P., Smith, W. K., Yuan, W., He, W., Lombardozzi, D., Kautz, M., Zhu, D., Lienert, S., Kato, E., Poulter, B., Sanders, T. G. M., Krüger, I., Wang, R., Zeng, N., Tian, H., Vuichard, N., Jain, A. K., Wiltshire, A., Haverd, V., Goll, D. S., and Peñuelas, J.: Recent Global Decline of CO2 Fertilization Effects on Vegetation Photosynthesis, Science, 370, 1295–1300, https://doi.org/10.1126/science.abb7772, 2020.

Weber, T., Haensler, A., Rechid, D., Pfeifer, S., Eggert, B., and Jacob, D.: Analyzing Regional Climate Change in Africa in a 1.5, 2, and 3 $\circ$C Global Warming World, Earth's Future, 6, 643–655, https://doi.org/10.1002/2017EF000714, 2018.

Williamson, G. B., Laurance, W. F., Oliveira, A. A., Delamônica, P., Gascon, C., Lovejoy, T. E., and Pohl, L.: Amazonian Tree Mortality during the 1997 El Niño Drought, Conservation Biology, 14, 1538–1542, https://doi.org/10.1046/J.1523-1739.2000.99298.X, 2000.

Winkler, A. J., Myneni, R. B., Alexandrov, G. A., and Brovkin, V.: Earth System Models Underestimate Carbon Fixation by Plants in the High Latitudes, Nature Communications, 10, 885, https://doi.org/10.1038/S41467-019-08633-Z, 2019a.

Winkler, A. J., Myneni, R. B., and Brovkin, V.: Investigating the Applicability of Emergent Constraints, Earth System Dynamics, 10, 501–523, https://doi.org/10.5194/esd-10-501-2019, 2019b.

Xiao, Z., Liang, S., Wang, J., Chen, P., Yin, X., Zhang, L., and Song, J.: Use of General Regression Neural Networks for Generating the GLASS Leaf Area Index Product From Time-Series MODIS Surface Reflectance, IEEE Transactions on Geoscience and Remote Sensing, 52, 209–223, https://doi.org/10.1109/TGRS.2013.2237780, 2014.

Xiao, Z., Liang, S., and Jiang, B.: Evaluation of Four Long Time-Series Global Leaf Area Index Products, Agricultural and Forest Meteorology, 246, 218–230, https://doi.org/10.1016/j.agrformet.2017.06.016, 2017.

Xu, L., Samanta, A., Costa, M. H., Ganguly, S., Nemani, R. R., and Myneni, R. B.: Widespread Decline in Greenness of Amazonian Vegetation Due to the 2010 Drought, Geophysical Research Letters, 38, https://doi.org/10.1029/2011GL046824, 2011.

Yang, Y., Saatchi, S. S., Xu, L., Yu, Y., Choi, S., Phillips, N., Kennedy, R., Keller, M., Knyazikhin, Y., and Myneni, R. B.: Post-Drought Decline of the Amazon Carbon Sink, Nature Communications, 9, 3172, https://doi.org/10.1038/S41467-018-05668-6, 2018.

Yuan, W., Zheng, Y., Piao, S., Ciais, P., Lombardozzi, D., Wang, Y., Ryu, Y., Chen, G., Dong, W., Hu, Z., Jain, A. K., Jiang, C., Kato, E., Li, S., Lienert, S., Liu, S., Nabel, J. E. M. S., Qin, Z., Quine, T., Sitch, S., Smith, W. K., Wang, F., Wu, C., Xiao, Z., and Yang, S.: Increased Atmospheric Vapor Pressure Deficit Reduces Global Vegetation Growth, Science Advances, 5, eaax1396, https://doi.org/10.1126/sciadv.aax1396, 2019.

Zhou, L., Tian, Y., Myneni, R. B., Ciais, P., Saatchi, S., Liu, Y. Y., Piao, S., Chen, H., Vermote, E. F., Song, C., and Hwang, T.: Widespread Decline of Congo Rainforest Greenness in the Past Decade, Nature, 509, 86–90, https://doi.org/10.1038/nature13265, 2014.

Zhu, Z., Bi, J., Pan, Y., Ganguly, S., Anav, A., Xu, L., Samanta, A., Piao, S., Nemani, R. R., and Myneni, R. B.: Global Data Sets of Vegetation Leaf Area Index (LAI)3g and Fraction of Photosynthetically Active Radiation (FPAR)3g Derived from Global Inventory Modeling and Mapping Studies (GIMMS) Normalized Difference Vegetation Index (NDVI3g) for the Period 1981 to 2011, Remote Sensing, 5, 927–948, https://doi.org/10.3390/rs5020927, 2013.

Zhu, Z., Piao, S., Myneni, R. B., Huang, M., Zeng, Z., Canadell, J. G., Ciais, P., Sitch, S., Friedlingstein, P., Arneth, A., Cao, C., Cheng, L., Kato, E., Koven, C., Li, Y., Lian, X., Liu, Y., Liu, R., Mao, J., Pan, Y., Peng, S., Peñuelas, J., Poulter, B., Pugh, T. A. M., Stocker, B. D., Viovy, N., Wang, X., Wang, Y., Xiao, Z., Yang, H., Zaehle, S., and Zeng, N.: Greening of the Earth and Its Drivers, Nature Climate Change, 6, 791–795, https://doi.org/10.1038/nclimate3004, 2016.